iScience

CellPress
OPEN ACCESS

Perspective

Unconventional van der Waals heterostructures beyond stacking

Peter Sutter[1,*] and Eli Sutter[2,*]

SUMMARY

Two-dimensional crystals provide exceptional opportunities for integrating dissimilar materials and forming interfaces where distinct properties and phenomena emerge. To date, research has focused on two basic heterostructure types: vertical van der Waals stacks and laterally joined monolayer crystals with in-plane line interfaces. Much more diverse architectures and interface configurations can be realized in the few-layer and multilayer regime, and if mechanical stacking and single-layer growth are replaced by processes taking advantage of self-organization, conversions between polymorphs, phase separation, strain effects, and shaping into the third dimension. Here, we highlight such opportunities for engineering heterostructures, focusing on group IV chalcogenides, a class of layered semiconductors that lend themselves exceptionally well for exploring novel van der Waals architectures, as well as advanced methods including in situ microscopy during growth and nanometer-scale probes of light-matter interactions. The chosen examples point to fruitful future directions and inspire innovative developments to create unconventional van der Waals heterostructures beyond stacking.

INTRODUCTION

The integration of dissimilar materials in heterostructures has long been a cornerstone of modern materials science. In the realm of conventional 3D crystalline materials, scientific discoveries such as interfacial electron gases and superconductivity in heterostructures of insulating oxides (Ohtomo and Hwang, 2004; Reyren et al., 2007) and applied technologies such as quantum well (Nakamura et al., 1997) and quantum cascade lasers (Faist et al., 1994) attest to the power of the concept of joining materials so that properties emerge that are no longer simply interpolations or linear combinations of those of the constituents but in many cases are dictated by few nanometer thin slices around interfaces.

Aside from enabling the exploration of the unique properties of atomically thin crystals, the advent of 2D materials such as graphene, hexagonal boron nitride, elementary 2D crystals in groups III to V, and ever-growing families of layered chalcogenides, pnictides and halides has provided new impetus to materials integration in heterostructures (Geim and Grigorieva, 2013; Novoselov et al., 2016). A unique advantage compared to 3D-crystalline materials is the easing of lattice-matching constraints when stacking 2D crystals, which originates in the weak (van der Waals) interaction between the individual layers. This implies that, in principle, arbitrary layer sequences of individual atomically thin membranes with large differences in lattice parameter and even entirely different in-plane crystal structures, covering materials ranging from metals to semiconductors and insulators, can be assembled by exfoliation from suitable bulk crystals and mechanical stacking (Liu et al., 2016). Alternatively, layers of the same 2D material can be stacked in non-equilibrium, azimuthally twisted configurations that give rise to exotic phenomena such as strong electron correlations and superconductivity (Cao et al., 2018; Wang et al., 2020), or novel optically excited quasiparticles such as moiré excitons (Jin et al., 2019; Seyler et al., 2019; Tran et al., 2019). While vertical van der Waals stacks benefit from a toolbox of numerous 2D crystals that are available by exfoliation, a second class of heterostructures joining different 2D crystals laterally within the same atomically thin membrane is a priori more difficult to realize since its fabrication requires bottom-up synthesis, given that in most cases no suitable bulk bicrystals exist for exfoliation. Despite this complication, and the constraint that the in-plane joined crystals need to be compatible and have limited lattice mismatch (Xie et al., 2018), lateral heterostructures with covalent line interfaces have been realized for many combinations of 2D crystals, including graphene-hBN (Levendorf et al., 2012; Sutter et al., 2014) and several combinations of transition metal dichalcogenide semiconductors (Duan et al., 2014; Gong et al., 2014; Huang et al., 2014b; Li et al., 2015).

[1]Department of Electrical & Computer Engineering, University of Nebraska-Lincoln, Lincoln, NE 68588, USA

[2]Department of Mechanical & Materials Engineering, University of Nebraska-Lincoln, Lincoln, NE 68588, USA

*Correspondence: psutter@unl.edu (P.S.), esutter@unl.edu (E.S.)

https://doi.org/10.1016/j.isci.2021.103050

This is an open access article under the CC BY-NC-ND license (http://creativecommons.org/licenses/by-nc-nd/4.0/).

Aside from vertical and lateral heterostructures, the two established forms of integrating 2D crystals, a rich diversity of layer and interface configurations can potentially open up as one transitions from one or a few atomic layers to thicker multilayer van der Waals crystals, assembled by bottom-up synthesis or subjected to post-growth processing. In this perspective, we examine some of the recent research directions into van der Waals heterostructures "beyond stacking". We first introduce an emerging class of van der Waals semiconductors, group IV chalcogenides, whose materials chemistry makes them uniquely suited as building blocks of unconventional heterostructures. Given the complexity of the underlying processes, in situ microscopy during growth and processing can facilitate understanding the role of phase conversion, phase separation, and other phenomena involved in heterostructure formation. Equally important are approaches for probing the emerging properties at the relevant length scales, which can be a significant challenge, for example when assessing light-matter interactions governed by a nanoscale volume near an interface. Following a brief primer on less-explored van der Waals materials, as well as methods for in situ microscopy and nanoscale optoelectronic/photonic measurements, the main part of this perspective discusses three unconventional avenues for integrating and shaping layered crystals: (i) van der Waals heterostructures obtained by phase conversion; (ii) heterostructures formed via phase separation; and (iii) and examples of 3D architectures of 2D/layered crystals. While not attempting to provide a comprehensive review, we are confident that a unified view of the status of the field can stimulate additional research along these emerging directions.

EMERGING VAN DER WAALS SEMICONDUCTORS FOR NOVEL HETEROSTRUCTURES, AND METHODS FOR PROBING THEIR GROWTH AND PROPERTIES

Cutting-edge research on van der Waals heterostructures has taken advantage of the high materials quality and flexibility afforded by mechanical exfoliation (Huang et al., 2015) and transfer methods (Frisenda et al., 2018). Using increasingly sophisticated transfer protocols, a majority of van der Waals stacks have been fabricated from a limited group of 2D crystals, including graphene, hexagonal boron nitride, and transition metal dichalcogenides (TMDs) MX_2, where M is a transition metal (frequently Mo or W) and X is one of the chalcogens S or Se. The same materials have also been the focus of efforts to develop bottom-up synthesis methods for heterostructures. Here, we emphasize a different class of 2D/layered crystals, group IV chalcogenides. As compounds of a group IV metalloid/metal (Ge, Sn) with S or Se, these semiconducting materials are not only of interest for a wide range of applications (as discussed below) but they have a defining crystallographic characteristic, the existence of multiple stable layered bulk crystal phases with different composition (i.e., chalcogen content and metal oxidation state), that makes them uniquely suitable for exploring the creation of novel heterostructures by bottom-up synthesis and post-growth processing.

Figure 1A illustrates this structural diversity for the example of the tin sulfides. The most sulfur-rich phase, tin disulfide (SnS_2), crystallizes in a trigonal CdI_2 structure (space group $P\bar{3}m1$) and the oxidation state of tin is Sn(IV). SnS_2 has an indirect bandgap between 2.06 eV (Julien et al., 1992) and 2.23 eV (Burton et al., 2016; Huang et al., 2014a) at room temperature and is naturally n-doped. Similar to the TMDs, the sulfur termination of the individual SnS_2 layers makes the material chemically inert so that it is readily exfoliated down to monolayer thickness (Huang et al., 2014a; Song et al., 2013) or synthesized as thin flakes (Su et al., 2015) down to a single atomic layer (Ye et al., 2017). Reported applications of SnS_2 include high-mobility, high on-off ratio field-effect transistors (FETs) (Huang et al., 2014a), FETs for sensing in aqueous solutions (Huang et al., 2018), photodetectors (Huang et al., 2014a, 2016; Zang et al., 2016), photocatalysts (Sun et al., 2012; Yu et al., 2014), and intercalation-type batteries (Gao et al., 2016). At the other end of the spectrum lies tin monosulfide (SnS), a compound analog of black phosphorus (Gomes and Carvalho, 2015; Xin et al., 2016) with anisotropic orthorhombic structure (space group Pnma) and Sn(II) cation oxidation state. Bulk SnS is a semiconductor with a reported fundamental bandgap between 1.1 and 1.3 eV (Ichimura et al., 2000; Parenteau and Carlone, 1990; Tanuševski and Poelman, 2003; Wang et al., 2012). Auto-doping due to acceptors believed to be Sn vacancies renders the material p-type (Tanuševski and Poelman, 2003), but processing can change the conductivity to n-type (Huang et al., 2013; Ristov et al., 1989). Orthorhombic α-SnS occurs naturally as the mineral herzenbergite, i.e., appears to be ambient-stable over geological time scales. Epitaxial growth on NaCl (Mariano and Chopra, 1967) or solution synthesis (Greyson et al., 2006) can stabilize SnS in a non-layered zincblende structure, and recent work has identified a cubic SnS phase with rocksalt-type structure (Rabkin et al., 2015). The open layer structure of layered monochalcogenides such as SnS has complicated both exfoliation as well as synthesis of ultrathin crystals, as shown by in situ microscopy of growth on van der Waals substrates (Sutter and Sutter, 2018), but ultrathin flakes

were obtained by moderating the surface reactivity by excess S (Sutter et al., 2020b, 2021c) and slow growth has yielded monolayers (Higashitarumizu et al., 2020). Due to its anisotropic puckered layer structure, SnS along with related monochalcogenides promises a number of extraordinary properties, for example for valleytronics (Lin et al., 2018) and piezo-/ferroelectrics (Fei et al., 2015, 2016; Higashitarumizu et al., 2020; Sutter et al., 2021c; Wu and Zeng, 2016). For the tin sulfides, an additional layered Sn_2S_3 phase exists with orthorhombic structure (space group Pnma), stoichiometry between that of SnS_2 and SnS, and mixed Sn(II)/Sn(IV) cation valence. With an anisotropic crystal structure of SnS_2-like, tilted layer fragments, bulk Sn_2S_3 is an n-type semiconductor with a fundamental bandgap of ~1.1 eV (Sanchez-Juarez and Ortiz, 2002). The existence of stable layered crystal phases with different composition suggests a facile conversion between these phases by controlling the chalcogen chemical potential. As we will discuss in more detail in later sections of this perspective, this characteristic creates opportunities for controlled heterostructure formation using different approaches, such as crystal transformations, phase separation, etc.

Besides compounds with different metal to chalcogen ratios, isostructural layered crystals with different cation and/or anion species provide further opportunities for materials integration in van der Waals heterostructures. Among the group IV chalcogenides, isostructural crystals across all combinations of cations and anions (M: Ge, Sn; X: S, Se) exist only for the monochalcogenides, MX. SnX_2 dichalcogenides crystallize with trigonal layered structures but have no equivalents in GeX_2, which either adopt other layered crystalline (Yang et al., 2018) or amorphous (glassy) structures (Phillips, 1979). The different monochalcogenides are illustrated in Figure 1B. Further diversity arises from the possibility of substitutional alloying, e.g., changes in the content of different anion species. Heterostructures of different group IV monochalcogenides are of particular interest due to the structural anisotropy of the constituent materials and the resulting anisotropic properties. As shown in Figure 1B, however, the anisotropic structure and the variations in lattice parameters can also complicate materials integration, notably in heterostructures with covalent interfaces in the plane of the layers, due to the anisotropic in-plane lattice mismatch between different monochalcogenide crystals. The combination of GeS and SnS, for example, involves a sizable lattice mismatch along the *a*-direction, $\frac{a^{SnS}-a^{GeS}}{a^{GeS}} = 9.7\%$, while the *b* lattice parameters closely match, $\frac{b^{SnS}-b^{GeS}}{b^{GeS}} = -0.3\%$.

While emerging materials such as group IV chalcogenides can become versatile building blocks for realizing van der Waals heterostructures by synthesis or post-growth processing, understanding the mechanisms of interface formation and probing the properties arising from the integration of 2D/layered crystals calls for advanced experimental techniques. Quantitative in situ microscopy promises fundamental insight into the microscopic processes involved in combining dissimilar materials. (Scanning) transmission electron microscopy ((S)TEM) at high temperatures provides direct imaging of atomistic processes but usually has limited capabilities for supplying gas- or vapor-phase species to drive crystal growth. On the other hand, techniques such as scanning electron microscopy (SEM) and low-energy electron microscopy (LEEM) provide in situ imaging at somewhat lower (few nanometers) resolution but facilitate the incorporation of deposition sources for real-time microscopy of growth. The capabilities of these different microscopy methods for imaging growth and transformations of 2D crystals and heterostructures are illustrated in Figure 2. Figure 2A shows in situ STEM of evolving reconstructions at edges of TMD monolayers (here $Mo_{1-x}W_x Se_2$, x = 0.05) (Sang et al., 2018). High-resolution STEM enables the identification of the atomic structures of preferred edge reconstructions, and real-time observations at high temperature capture the simultaneous evolution of the edge shape and reconstruction toward a nanowire-terminated ZZSe-Mo-NW30 edge under Mo-rich conditions.

Using a focused electron beam to excite secondary electrons that are detected for imaging, environmental SEM provides versatile in situ imaging capabilities during exposure to gases or vapors at variable temperature. The image acquisition using a scanned electron beam limits the temporal resolution to a few seconds while a spatial resolution down to ~3 nm is realized with field-emission electron sources. Typical electron energies are ~5 keV. With these characteristics in situ SEM can be used to analyze the nucleation and growth of 2D crystals on conducting substrates, as illustrated for the example of graphene growth on polycrystalline Cu foils in Figure 2B, where growing hexagonal graphene domains are visible with strong contrast against the metal substrate (Wang et al., 2015). LEEM, finally, differs in several respects from both STEM and SEM (Bauer, 2020; Sutter and Sutter, 2013). First, the sample is illuminated by a wide collimated electron beam, and counter-propagating backscattered electrons are collected for imaging.

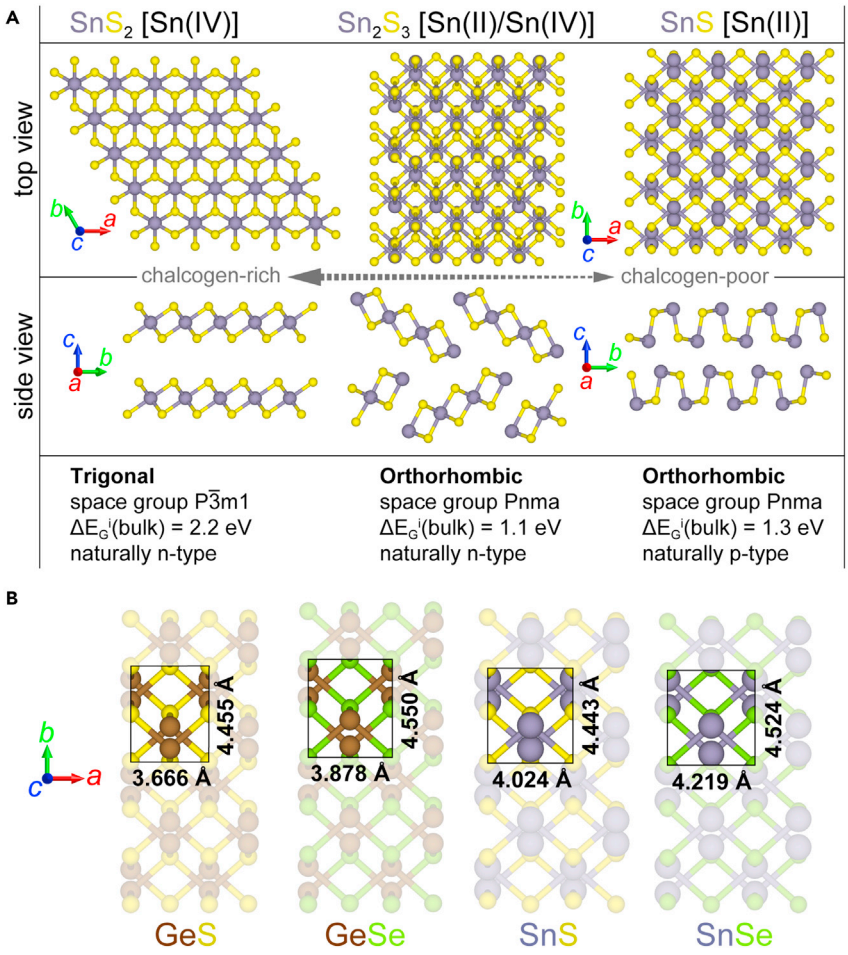

Figure 1. Van der Waals crystals for unconventional heterostructures

(A) Structurally diverse Sn sulfides as building blocks for van der Waals heterostructures. Stable bulk crystals include the dichalcogenide SnS_2 and monochalcogenide SnS, as well as a Sn_2S_3 structure with intermediate stoichiometry and mixed Sn(II)/Sn(IV) cation valence.

(B) Anisotropic group IV monochalcogenides. Isostructural layered crystals with stoichiometry MX (M: Ge, Sn; X: S, Se) provide opportunities for integration of materials with anisotropic lattice mismatch and properties. Rectangles outline the in-plane unit cells of the different orthorhombic MX crystals. Relaxed lattice parameters along the *a* and *b* crystal axes represent values computed by density functional theory (Jain et al., 2013).

Secondly, LEEM uses very low electron energies, typically between 0 and 100 eV. Full-field imaging enables high frame rates (video rate, i.e., ~10–20 frames per second), while low electron energies ensure damage-free and highly surface-sensitive imaging, where the signal originates from within a few atomic layers of the sample surface. Conventional low-energy electron microscopes reach ~7 nm spatial resolution while aberration-corrected instruments achieve imaging with resolution below 2 nm. Together with ultrahigh vacuum base pressure, versatile deposition from gas, vapor, or molecular beam sources, widely variable sample temperatures (180 K to over 1500 K), and a number of analytical modes (low-energy electron diffraction [LEED]; surface potential/workfunction imaging; photoelectron spectroscopy; angle-resolved photoelectron spectroscopy, etc.), these characteristics are ideal for real-time microscopy of 2D crystal and heterostructure growth, as well as processing. Figure 2C illustrates the application of LEEM to real-time microscopy of 2D crystal growth, using the example of macroscopic graphene growth on Ru(0001) driven by carbon segregation from the metal substrate. Bright-field LEEM not only shows contrast between pristine and graphene-covered regions but also visualizes atomic steps on the support via Fresnel interference (Chung and Altman, 1998). The combination of both types of image contrast was crucial in identifying a carpet-like expansion of intact graphene sheets across substrate steps, which enables the expansion of the graphene domains to macroscopic size (Sutter et al., 2008).

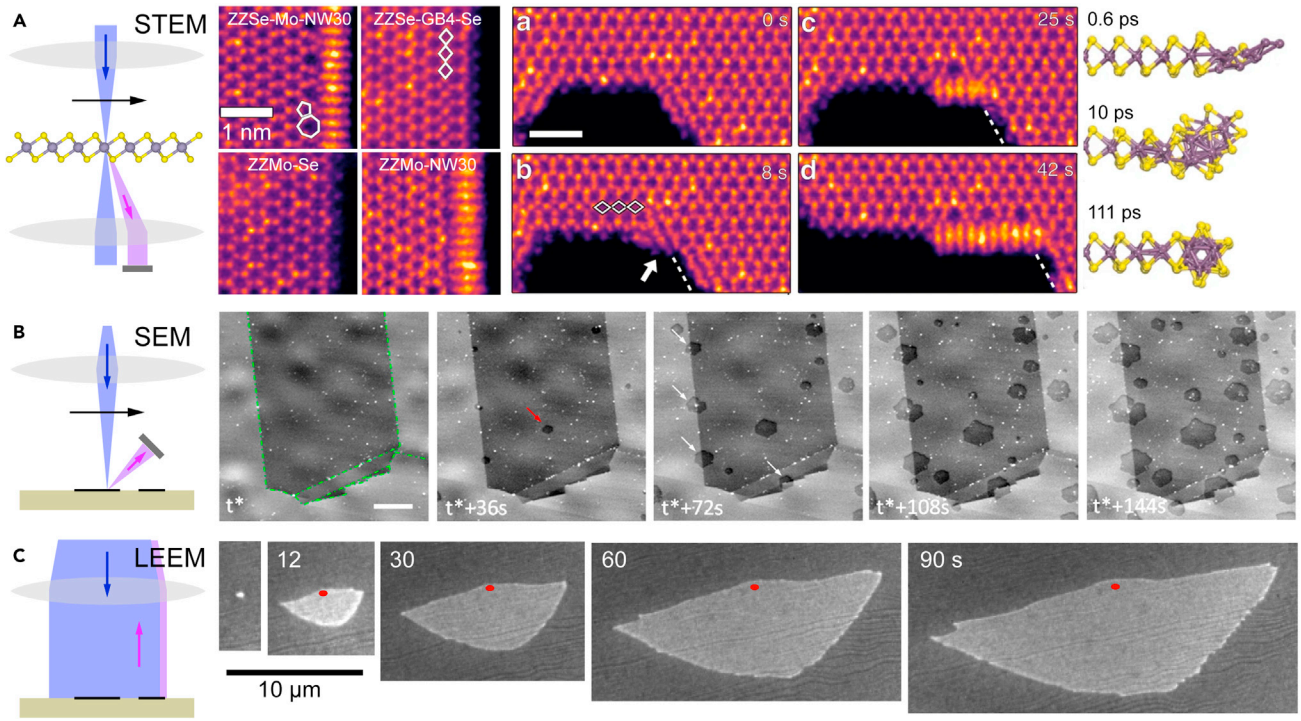

Figure 2. In situ microscopy of growth and transformations of 2D crystals and heterostructures

(A) Scanning transmission electron microscopy (STEM) provides atomic-resolution imaging at high temperatures, as illustrated by dynamic observations of evolving edge reconstructions of $Mo_{0.95}W_{0.05}$ Se_2 monolayers at 500°C. Adapted from Sang et al. (2018). Copyright 2018 Springer Nature.

(B) Environmental scanning electron microscopy (SEM) provides mesoscale imaging during 2D/layered crystal growth at high temperatures and during exposure to gases or vapors, as illustrated by observations of graphene growth on Cu foils at 1000°C. Scale bar: 5 μm. Adapted from Wang et al. (2015). Copyright 2015 American Chemical Society.

(C) Low-energy electron microscopy (LEEM) enables real-time microscopy of growth and processing of 2D/layered crystals and heterostructures during exposure to vapors or gases at high temperature, as illustrated by the observation of macroscopic graphene growth on Ru(0001) at 850°C. Adapted from Sutter et al. (2008). Copyright 2008 Springer Nature.

Novel electronic, optoelectronic, and photonic characteristics defined by interface formation between the same or dissimilar materials are among the most exciting emerging properties of van der Waals homo- and heterostructures. Most properties of vertical van der Waals stacks obtained by exfoliation and transfer methods can be interrogated using approaches that offer micrometer-scale resolution, such as diffraction-limited far-field optical spectroscopy, sufficient to accommodate the often small (few μm) sample sizes. Examples of such measurements include micro-Raman and photoluminescence (PL) spectroscopy (Splendiani et al., 2010), ellipsometry (Funke et al., 2016), absorption (Havener et al., 2013) or photocurrent spectroscopy (Nazin et al., 2010), modulation spectroscopies such as thermoreflectance (Ho et al., 2004), etc. Probing laterally heterogeneous structures, on the other hand, is complicated by the requirement for measurements with high spatial resolution, matching the characteristic length scale within the sample plane. Examples of such systems include lateral heterostructures of 2D crystals and interlayer twist moirés. In lateral heterostructures, different 2D materials are covalently joined (or "stitched") in the plane, thus generating an often atomically sharp line interface. Such structures were first synthesized from the honeycomb crystals graphene and hexagonal boron nitride (h-BN) (Levendorf et al., 2012; Sutter et al., 2012), and later from different combinations of TMDs such as MoS_2–WS_2 (Gong et al., 2014), $MoSe_2$–WSe_2 (Huang et al., 2014b), and MoS_2–WSe_2 (Li et al., 2015). Sharp lateral interfaces set a natural length scale of the order of 1 nm, and probing emerging optoelectronic phenomena, e.g., spatially indirect excitons, at such interfaces clearly requires advanced methods beyond the conventional diffraction-limited spectroscopies. Similarly, interlayer moiré patterns generated by twisted stacking of 2D crystals modulate the electronic and optoelectronic properties within the plane. Twisted van der Waals crystals and interlayer moirés have attracted significant interest due to phenomena such as flat electronic bands (i.e., zero Fermi velocity) and resulting strong electron correlations (e.g., in twisted bilayer graphene (Cao et al., 2018) and

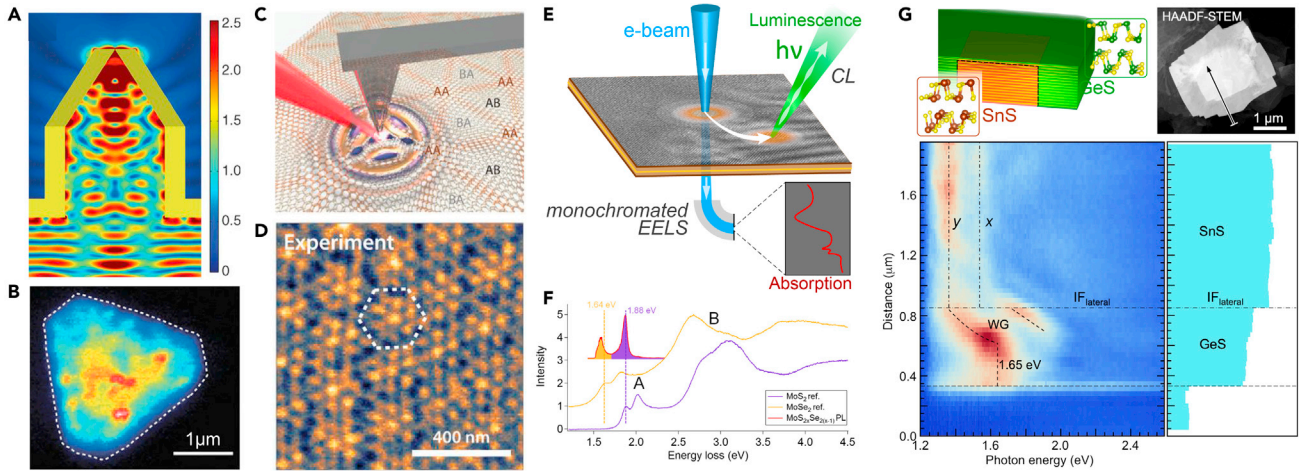

Figure 3. Sub-diffraction optoelectronics and photonics in van der Waals crystals and heterostructures. (A and B) Aperture SNOM.
(A) Efficient bidirectional coupling between macroscopic and nanometer length scales in shaped plasmonic SNOM probes. Adapted from Bao et al. (2012). Copyright 2012 American Association for the Advancement of Science.
(B) Luminescence mapping of a single-layer MoS_2 flake shows nanoscale heterogeneity at the flake edges and locally in the interior. Adapted from Bao et al. (2015). Copyright 2015 Springer Nature.
(C and D) Scattering SNOM. (C) Schematic of a setup for nano-infrared (IR) imaging of plasmon polaritons in twisted bilayer graphene.
(D) Nano-IR amplitude image for a plasmon polariton wavelength λ_p = 135 nm, demonstrating the periodic variations in the optical response arising from the modification of the electronic structures at moiré domain walls (solitons) in rotationally misaligned graphene layers. Adapted from Sunku et al. (2018). Copyright 2018 American Association for the Advancement of Science.
(E-G) Nano-optoelectronics in scanning transmission electron microscopy (STEM). (E) Schematic of cathodoluminescence (CL) and electron energy-loss spectroscopy (EELS), two major types of electron beam excitation and detection suitable for probing optoelectronics and photonics at the nanoscale.
(F) Local absorption measurements using monochromated EELS in MoS_2 and $MoSe_2$ parts of a heterogeneous $MoS_{2x}Se_{2(1-x)}$ monolayer, compared with a spatially averaged photoluminescence spectrum of the same sample. Adapted from Tizei et al. (2015). Copyright 2015 American Physical Society.
(G) Schematic and STEM image of a lateral heterostructure between multilayer SnS and GeS (top); hyperspectral CL linescan and corresponding STEM intensity profile across the lateral GeS-SnS interface (bottom). Adapted from Sutter et al. (2020a). Copyright 2020 American Chemical Society.

twisted bilayer TMDs (Wang et al., 2020)), moiré excitons (Jin et al., 2019; Tran et al., 2019) and moiré-trapped valley excitons (Seyler et al., 2019). Here the characteristic lateral length scale of the order of the moiré unit cell size can vary between a few nanometers at large angles up to a few hundred nanometers at small twist angles, i.e., can again fall substantially below the diffraction limit. Scanning tunneling microscopy and spectroscopy (STM, STS) is the method of choice for probing local electronic structure phenomena in such laterally inhomogeneous van der Waals systems, e.g., local quasiparticle bandgaps and interfacial band offsets in lateral heterostructures (Zhang et al., 2018) or potential variations across twist moiré superlattices (Shabani et al., 2021).

Probing optoelectronics at length scales far below the diffraction limit presents complications that have been addressed in two different ways: (i) by near-field optical methods; and (ii) using excitation by a focused electron beam. In scanning near-field optical microscopy (SNOM) field enhancements by a tip, held in close proximity to the sample surface and raster-scanned across the field of view, are used to obtain imaging with resolution below the diffraction limit. The tip-sample junction can be excited either through a transparent probe (aperture SNOM) or by focusing light from an external source onto the apex of a metallic tip and detecting scattered light from the tip-sample junction (scattering SNOM). Sub-diffraction hyperspectral imaging in aperture SNOM with shaped plasmonic probes (Figure 3A) has been applied to obtain sub-micrometer resolved luminescence maps of monolayer TMD semiconductors (Figure 3B), identifying heterogeneity in the form of distinct optoelectronic systems corresponding to a pristine interior, disordered edges, as well as intra- and interflake grain boundaries (Bao et al., 2015). Scattering SNOM provides additional advantages, such as compatibility with a broad spectrum of excitation energies to the mid-infrared and THz range, limited only by the availability of suitable light sources and detectors. The technique has been used widely to investigate hybrid light-matter states in 2D crystals, including plasmon polaritons in graphene (Dai et al., 2019), phonon polaritons in h-BN (Ni et al., 2018), and exciton polaritons in multilayer TMDs (Hu et al., 2017). Figures 3C and 3D show a recent example demonstrating the

achievable spatial resolution in heterogeneous 2D materials, here moiré superlattices in twisted bilayer graphene. The appearance of chiral 1D states across moiré domain walls causes a local enhancement of the optical conductivity in the form of a periodic photonic crystal for plasmons, which produces interference patterns whose structure depends on the (gate-tunable) plasmon wavelength (Figure 3D).

Fundamentally different approaches toward optoelectronic spectroscopy and nanophotonics far below the diffraction limit are offered by electron microscopy. In STEM, for example, passage of a focused (~1 nm) relativistic electron beam can create both electronic excitations (García de Abajo, 2010) and launch propagating modes in photonic waveguides (Sutter et al., 2018, 2021b), while the response can be probed either by analyzing electron energy losses (electron energy loss spectroscopy, EELS) or by detecting emitted electromagnetic radiation (cathodoluminescence, CL; Figure 3E). EELS in monochromated STEM, where the energy spread of the incoming electron beam is reduced from ~0.3 eV or ~0.8 eV typical of cold field emitter and Schottky cathodes, respectively, to below 20 meV using a monochromator (Krivanek et al., 2014), provides access to optical absorption measurements at the nanometer scale. By recording low-loss EEL spectra, optical bandgaps and excitonic absorption spectra can be obtained. Figure 3F illustrates this capability with measurements of excitonic spectra in MoS_2 and $MoSe_2$ regions of a heterogeneous $MoS_{2x}Se_{2(1-x)}$ monolayer (Tizei et al., 2015). In absence of a background from the narrow zero-loss peak, two sharp peaks between 1.5 and 2.1 eV, corresponding to the spin-orbit split A-exciton, and a broader peak at around 3.0 eV matching the B-exciton, are observed. Recent work has extended these capabilities to measuring exciton dispersions in monolayer TMDs by momentum-resolved EELS (Hong et al., 2020) and using the lifetime broadening of the excitonic losses in EELS to track interlayer charge transfer rates in twisted TMD bilayers (Gogoi et al., 2019).

While monochromated EELS provides local optical absorption measurements, the detection of emitted light in CL can involve additional excitation transfers away from the position of the exciting electron beam. Influenced by transport phenomena such as electron-hole pair or exciton diffusion, drift of charged excitons in electric fields and carrier separation at interfaces, CL spectra can have nonlocal character. Figure 3G illustrates this for the example of electron-hole pair separation near a lateral interface between multilayer GeS and SnS, visualized through hyperspectral CL linescans across the two components and the interface. On the SnS side far from the interface, CL spectra show a characteristic pair of luminescence peaks corresponding to the bandgaps along the *x* and *y*-valleys in SnS (Lin et al., 2018). Close to the interface the lower energy (1.35 eV) *x*-valley emission is strongly quenched while the (1.55 eV) *y*-valley peak retains a constant intensity, indicating a valley-selective carrier separation at the lateral GeS-SnS interface (Sutter et al., 2020a). Besides optoelectronics, CL can also be used to probe nanophotonics in 2D/layered crystals and heterostructures, based on the ability of the focused high-energy electron beam to induce propagating photonic modes in layered semiconductors down to the ultrathin limit.

CREATING VAN DER WAALS HETEROSTRUCTURES BY PHASE CONVERSION

Two-dimensional transition metal dichalcogenides typically adopt a constant composition (MX_2) but nevertheless can crystallize in different structures (or polymorphs). Seamlessly stitching different polymorphs within the same monolayer provides a powerful approach to materials integration. A classic example of this "phase engineering" paradigm toward 2D heterostructures is the conversion between the trigonal prismatic (semiconducting) 2H and the octahedral (metallic) 1T polymorphs of MoS_2. Liquid-phase exfoliation of MoS_2 using organolithium intercalation leads to mixed monolayers in which the 2H and 1T phases coexist in compact nanoscale domains connected by atomically sharp interfaces (Eda et al., 2012). The 1T phase is stabilized by electron donation from organolithium during intercalation (Py and Haering, 1983) and remains as a metastable phase even after complete organolithium removal. These findings suggest the possibility of patterning heterostructures where, starting from pure 2H MoS_2, local electron donation causes the controlled conversion to the 1T phase in the patterned regions. This concept was successfully realized by using lithographic patterning to define a protective photoresist cover across the desired 2H regions and exposing the uncovered MoS_2 to n-butyl lithium at room temperature, followed by washing steps to remove the organic and lithium ion residues (Kappera et al., 2014). The metallic 1T phase could subsequently be used as low-resistance source and drain contacts in FETs with 2H-MoS_2 channels, demonstrating the utility of phase engineering for electronic device applications. Since the 2H to 1T phase conversion can be achieved by electron donation, electron-beam irradiation provides an alternative way of depositing sufficient negative charge to drive the transformation. Besides in situ TEM during lithium intercalation (Wang et al., 2014), this alternative pathway opened up the possibility of observing the underlying

atomistic processes in monolayers using low-voltage STEM (Lin et al., 2014). STEM imaging at high temperatures shows the elementary steps leading up to the S-plane gliding at the heart of the 2H to 1T transformation, beginning with the formation of narrow bands of a precursor of constricted MoS_2 zigzag chains surrounded by the 2H-MoS_2 host. Strain at corners between these bands triggers Mo-S glide to form a triangular nucleus of the 1T phase, which then expands via secondary boundary structures that mediate the further gliding of the crystal planes.

Whereas for TMDs multiple polymorphs exist with the same composition, the Sn chalcogenides introduced above harbor several stable phases with different stoichiometry. Phase conversions across the full range of stable layered crystal phases from SnX_2 (X: S, Se) to SnX can be driven by adjusting the chalcogen chemical potential, μ_S (or μ_{Se}). The transformations can occur in both directions and are reversible. The conversion from SnS_2 to SnS has been driven thermally (e.g., by laser annealing (Voznyi et al., 2016)) and by plasma-induced S removal (Kim et al., 2018a). High-energy electron irradiation can drive a controlled chalcogen removal and thus initiate the formation of S vacancies culminating in the complete transformation of few-layer SnS_2 into SnS (Figures 4A and 4B, (Sutter et al., 2016)). By restricting the area exposed to the electron beam, lateral heterostructures of SnS embedded in an SnS_2 matrix (or analogous structures of the corresponding selenides) can be obtained. Driving the transformation by knock-on sulfur removal in TEM enables in situ observations of the process, both at room temperature and at elevated temperatures (Figure 4C). SnS_2 crystals with different thickness are converted to SnS domains in which the orientation of the van der Waals interfaces is either preserved (ultrathin 1–3 ML SnS_2) or tilted by 21° (few-layer SnS_2, Figure 4D). Calculations show that these differences arise from different transformation pathways. In few-layer SnS_2 the introduced sulfur vacancies interact to form vacancy lines, which in turn enable a rotational realignment of the intervening crystalline segments into a local Sn_2S_3 structure that templates the tilt of the final SnS phase. In the ultrathin limit the Sn_2S_3 intermediate is geometrically inaccessible and the product is basal-plane oriented SnS (Sutter et al., 2016). The transformation of $SnSe_2$ generally proceeds analogously, beginning with the disruption of long-range order in the $SnSe_2$ layers and followed by the appearance of an ordered SnSe lattice. However, the final SnSe phase invariably consists of basal-plane oriented layers parallel to those of the $SnSe_2$ mother crystal, consistent with the absence of a stable intermediate Sn(II)/Sn(IV) phase (equivalent to Sn_2S_3) in the selenides (Sharma and Chang, 1986). These results open up a number of avenues toward functional van der Waals heterostructures. Ultrathin SnS_2, for instance, can be converted into laterally stitched heterostructures forming electronically active junctions between p-type SnS and n-type SnS_2. Here key questions, such as the possible ways of accommodating the structural mismatch created by joining orthorhombic and trigonal layered crystals, remain unanswered. The conversion of thicker few-layer SnS_2 also creates interesting possibilities since it leads to tilted SnS projecting an abundance of chemically reactive edge sites embedded in a SnS_2 membrane. This scenario has evident ramifications for applications in catalysis and photocatalysis, but the functional properties of such tilted-layer heterostructures remain unexplored.

The inverse process, namely the reaction SnS + S → SnS_2 under chalcogen-rich conditions has been pursued for the bottom-up synthesis of twisted van der Waals stacks. In such materials, interlayer twist – an in-plane rotation of the layers – produces an interfacial moiré superlattice that modifies the electronic and optoelectronic properties. Twisted bilayer graphene, for instance, shows flat-band induced strongly correlated electron behavior including gate tunable Mott insulator and superconducting phases at small "magic" twist angles (Cao et al., 2018). Twisted TMD bilayers exhibit similar correlation effects (Wang et al., 2020), as well as many-body excitations such as moiré excitons (Jin et al., 2019; Seyler et al., 2019; Tran et al., 2019). While precision mechanical stacking has been the approach of choice for producing twisted stacks (Kim et al., 2016; Yang et al., 2020), growing them by van der Waals epitaxy is complicated by the strong affinity toward (aligned) equilibrium stacking (Woods et al., 2016). A recently proposed rational approach for locking in non-equilibrium stacking arrangements during growth involves a two-step process in which the synthesis of an intermediate 2D (or 3D) crystalline phase (**B**) on a layered substrate (**A**) is followed by the conversion of the intermediate to a final phase $\mathbf{A}^{rot}$ with a defined azimuthal rotation relative to the substrate (Figure 4E) (Sutter et al., 2019c). This method was initially demonstrated for the synthesis of graphene bilayers with 30° twist angle, using hBN as an (isostructural) intermediate 2D crystal. hBN, which grows in an R0° configuration on SiC, was transformed by annealing into a graphene layer with the same R0° orientation; a second graphene layer was then grown by thermal decomposition of SiC in the usual R30° orientation, thus forming bilayer graphene with precise 30° interlayer twist (Ahn et al., 2018). Although not directly relevant to moiré physics, such 30°-twisted bilayers are of interest since

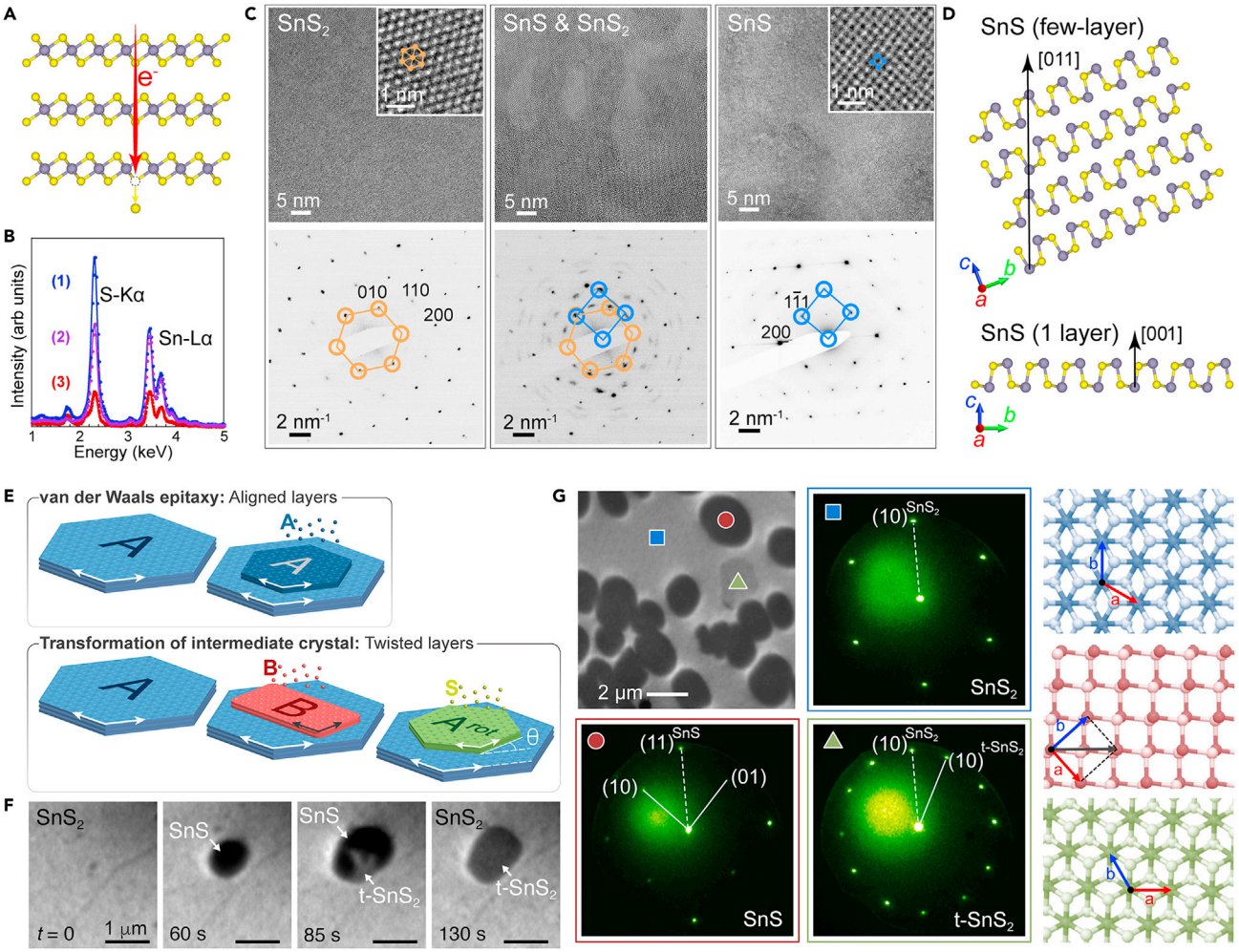

Figure 4. Tin chalcogenide heterostructures via phase conversion

(A–D) Electron-beam-induced transformation of SnS_2 into SnS suspended in a SnS_2 matrix. (A) Schematic of the electron-beam-induced (knock-on) generation of S vacancies. (B) EDS spectra documenting the change in composition from SnS_2 to SnS, (1)–(2), followed by a global signal reduction indicating thinning by the electron beam, (2)–(3). (C) TEM images and electron diffraction patterns obtained during the electron beam-induced SnS_2 to SnS transformation. (D) Thickness-dependence of the final SnS morphologies after the transformation. Adapted from Sutter et al. (2016). Copyright 2016 American Chemical Society.

(E–G) Bottom-up synthesis of twisted chalcogenides. (E) Comparison of ordinary van der Waals epitaxy and of a two-step process yielding twisted layer stacks. (F) In situ LEEM of the spontaneous formation of 30°-twisted t-SnS_2 by growth and transformation of azimuthally aligned SnS on an SnS_2 substrate. (G) Phase identification by local low-energy electron diffraction (micro-LEED): SnS_2 substrate (blue); SnS azimuthally aligned with the SnS_2 substrate, where $(11)^{SnS} \parallel (10)^{SnS_2}$ (red); and 30°-twisted t-SnS_2 (green). Adapted from Sutter et al. (2019c). Copyright 2019 Springer Nature.

they realize a 2D Stampfli-tiling dodecagonal quasicrystal (Stampfli, 1986). The two-step protocol shown in Figure 4E was successfully used to create twisted chalcogenide semiconductors by relying on transformations between different tin sulfide phases (Sutter et al., 2019c). Here, the substrate (**A**) is SnS_2 and the intermediate 2D phase (**B**) consists of ultrathin SnS. Despite the structural mismatch between orthorhombic SnS and trigonal SnS_2 (see Figure 1A), in situ microscopy using LEEM showed growth of the SnS intermediate with a well-defined, fixed azimuthal orientation relative to the SnS_2 support. During growth, the SnS domains spontaneously transform to SnS_2 that is 30° twisted relative to the underlying SnS_2 (Figures 4F and 4G). Continued SnS deposition leads to a repetition of the process, where new SnS domains nucleate preferentially on t-SnS_2/SnS_2 stacks. This leads to a self-organized alternation of SnS_2 layers with 0° and 30° orientation, promising an avenue toward the synthesis of complex SnS_2 twist superlattices. In the processes shown in Figures 4E–4G, a key question concerns the origin of the excess S needed to induce sulfur-rich conditions and spontaneously convert the SnS intermediate to SnS_2. For growth on SnS_2, the substrate

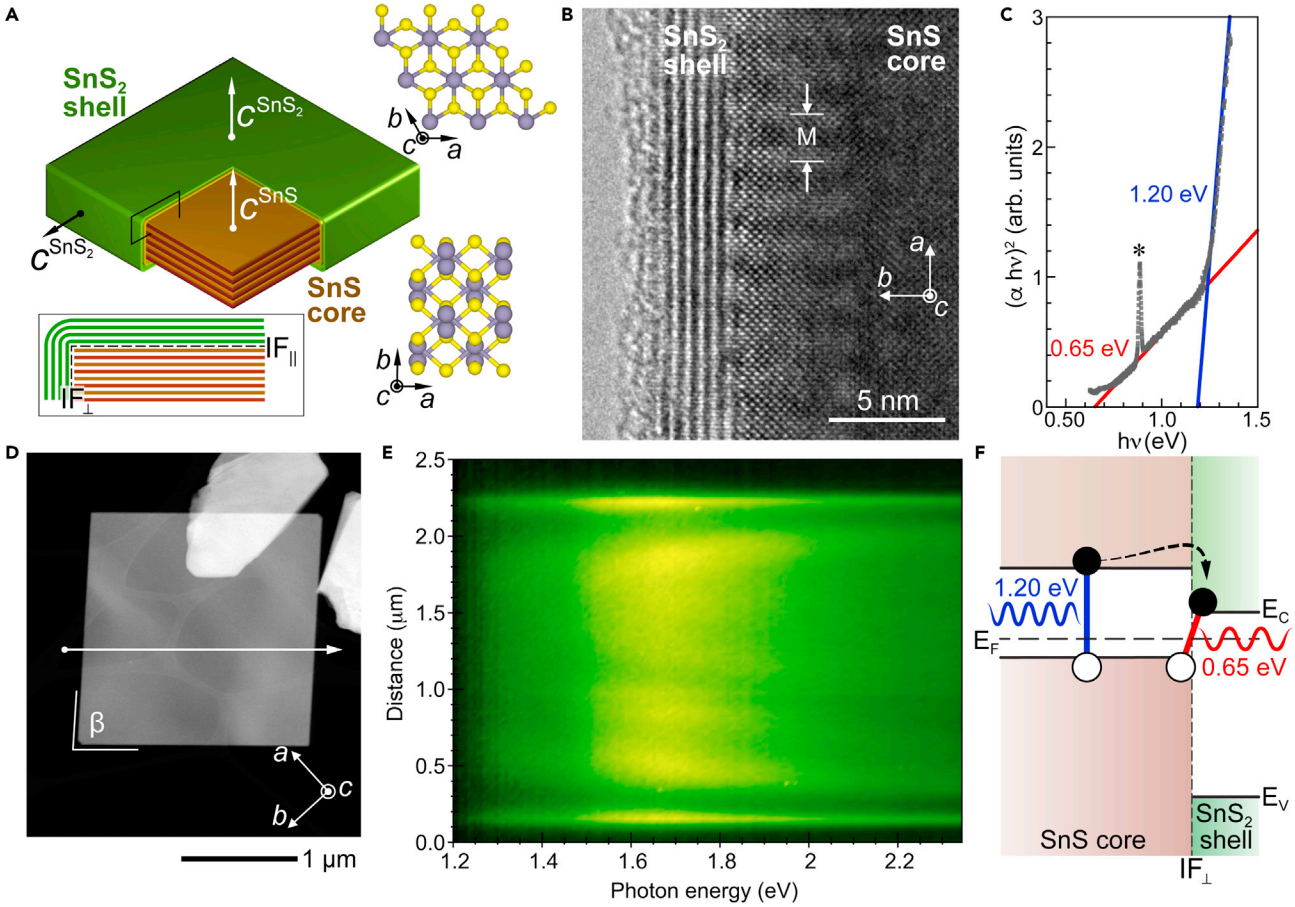

Figure 5. Wrap-around core–shell heterostructures via spontaneous phase separation of structurally incompatible van der Waals crystals

(A) Schematic of SnS–SnS_2 wrap-around core-shell heterostructures formed during SnS growth with a small excess of sulfur. The core-shell geometry involves two-types of van der Waals interfaces, with $IF_{\parallel}$ corresponding to ordinary van der Waals stacking along the top and bottom facets while $IF_{\perp}$ along the side facets consists of orthogonal core and shell layering.

(B) High-resolution TEM near the core-shell interface, showing the layered SnS_2 shell tightly enclosing the SnS core. M: Moiré structure due to superposition of the lattices of the SnS core and of the crystalline SnS_2 shell.

(C) Tauc plot obtained by UV-Vis absorption on a dense array of wrap-around core-shell flakes, showing two distinct absorption onsets at 1.20 eV and 0.65 eV, respectively.

(D) STEM image of a SnS–SnS_2 wrap-around core-shell structure. Axes identify the SnS lattice directions.

(E) Hyperspectral CL linescan along the arrow in D, showing luminescence quenching near the $IF_{\perp}$ core-shell interface.

(F) Band diagram illustrating the type II band offset (responsible for charge separation, dashed arrow), band-to-band absorption in SnS, and interfacial (spatially indirect) absorption at the core-shell interface. Adapted from Sutter et al. (2019d). Copyright 2019 Wiley-VCH.

acts as a reservoir that thermally liberates S at the growth temperature. SnS growth on other supports that do not readily release chalcogens, such as MoS_2 and WS_2, again produces orthorhombic SnS domains that are azimuthally aligned with the underlying trigonal crystal lattice. The SnS can then be converted to twisted t-SnS_2 on TMDs by supplying sulfur from an external source at elevated temperature (Sutter et al., 2019c).

VAN DER WAALS HETEROSTRUCTURES VIA PHASE SEPARATION

In addition to transformations between different layered crystal phases, the structural conflict created by the coexistence (or co-deposition) of structurally incompatible (non-isotypic) phases can also provide a powerful stimulus for the formation of van der Waals heterostructures. Figure 5 illustrates this for the example of the tin chalcogenides SnS and SnS_2. As discussed above, excess sulfur (i.e., a large chemical potential of the chalcogen) can convert orthorhombic SnS into trigonal SnS_2. By tuning the conditions of a one-pot synthesis process so that SnS is evaporated along with only a small amount of excess S, a

complete transformation of the growing flakes to SnS_2 is avoided. Instead, such a process leads to the crystallization of a SnS majority phase jointly with a SnS_2 minority phase. The incompatible crystal structures favor a phase separation of SnS and SnS_2. In principle, this phase separation could lead to separate SnS and SnS_2 flakes or well-known heterostructure morphologies, such as vertical stacks of the two van der Waals crystals. Instead, a striking new type of van der Waals architecture is spontaneously formed: dense arrays of core-shell heterostructure flakes in which large orthorhombic SnS crystals are enclosed in a wrap-around shell of trigonal SnS_2 (Figures 5A and 5B) (Sutter et al., 2019d). The tightly wrapped layered SnS_2 shell forces two types of interfaces to the SnS core. While the top and bottom facets contain regular van der Waals interfaces between parallel SnS and SnS_2 layer stacks ($IF_{\parallel}$), the side facets contain unconventional interfaces with orthogonal SnS and SnS_2 layers ($IF_{\perp}$). The thickness of the SnS_2 shell could be further enlarged by annealing in a sulfur-rich atmosphere, demonstrating the tunability of the core–shell heterostructures using post-growth processing.

Abundant interfaces generating type II SnS/SnS_2 heterojunctions (Whittles et al., 2016) govern the optoelectronic properties of the wrap-around core-shell heterostructures. Optical absorption measurements in the near-infrared wavelength range, represented by Tauc plots in Figure 5C, indicate two distinct absorption onsets at 1.2 eV and 0.65 eV, respectively. The higher-energy onset corresponds to band-to-band transitions in the SnS core, while the energy of the second absorption edge is consistent with a spatially indirect interfacial absorption process that generates pairs of electrons and holes localized on different sides of the interface. CL spectroscopy with nanometer spatial resolution gives evidence for an anisotropic charge separation, which behaves as in ordinary van der Waals stacks near the $IF_{\parallel}$ (top, bottom) interfaces but shows substantially increased carrier collection distances within the core layers near the unusual $IF_{\perp}$ interfaces at the lateral edges of the heterostructures (Figures 5D and 5E). Since the SnS_2 terminating the surface of the heterostructures is a visible-light photocatalyst, these findings suggest enhanced light harvesting for photocatalysis and photo-electrochemistry through absorption by the core and shell as well as the exceptionally abundant (wrap-around) interfaces, which jointly cover the visible spectrum and reach into the near-infrared to energies far below the bandgaps of the individual semiconductors. More broadly, this case study using tin chalcogenides as a model system suggests the existence of a vast, as yet unexplored playground for the formation of novel van der Waals heterostructures by exploiting the co-deposition of incompatible layered crystals and adjusting the growth conditions so as to tune phenomena such as spontaneous phase separation.

One might expect that a similar one-pot synthesis under chalcogen-rich conditions of other group IV chalcogenides shown in Figure 1B would similarly lead to MX-MX_2 wrap-around core-shell structures. Such an extension of the process has so far been reported for GeS growth from a slightly S-rich precursor (Sutter et al., 2019b). Vapor-transport growth at substrate temperatures between 320 and 350°C produces few-layer to multilayer GeS flakes that show anisotropic vibrational properties. TEM indeed shows a core–shell structure, in which single-crystalline GeS crystals are wrapped in a continuous sulfur-rich shell. However, since GeS_2 is a glass former, the shells surrounding the GeS cores are amorphous. Similar to the case of tin chalcogenides, germanium sulfide acquires special properties in GeS-*a*GeS_2 core–shell structures. CL again shows charge separation consistent with a staggered-gap (type II) interface between core and shell. Even more striking are the effects on chemical stability. Control experiments with pure GeS exfoliated from bulk crystals showed the onset of severe chemical degradation within a few hours, likely as a result of hydrolysis in humid air (Rochow and Abel, 1973), accompanied by signatures in PL and X-ray photoelectron spectroscopy that indicate the formation of nonstoichiometric Ge oxides (GeO_x, $1 < x < 2$). In contrast, the synthetic GeS-*a*GeS_2 core-shell structures were found to be long-term stable when exposed to air. Optical and atomic force microscopy show no detectable changes after prolonged exposure to air (several months to over 1 year) (Sutter et al., 2019b). These findings are consistent with the reported stability of GeS_2 chalcogenide glasses in air (Kim et al., 2008). Hence, while materials exfoliated from bulk crystals are often perceived as crystals of the highest possible quality, vapor-transport grown GeS with a spontaneously formed protective sulfur-rich shell stands out with its superior long-term chemical stability. In this way, the self-passivated synthetic GeS is superior to exfoliated GeS flakes; in addition, the functional properties of the GeS-*a*GeS_2 flakes are at least on par with materials derived from high-quality single crystals. For example, nanometer-scale CL spectroscopy shows minority carrier (electron) diffusion lengths in the p-type GeS core of ~0.27 μm (Sutter et al., 2019b), comparable to the diffusion lengths in the highest-quality layered TMD semiconductors (Cadiz et al., 2018; Kim et al., 2018b).

2D GOES 3D

Along the path of scientific discovery planar 2D crystals have emerged relatively recently, in many cases following on the heels of earlier studies on curved polymorphs of the same materials. This is the case for sp^2 carbon allotropes, where extensive studies on fullerenes such as C60 (Kroto et al., 1985) and carbon nanotubes (Iijima, 1991) preceded concerted efforts at exploring the planar form, graphene (Novoselov et al., 2004). Incidentally, the same is not true for transition metal dichalcogenides, where planar monolayers were obtained by liquid-phase exfoliation (Joensen et al., 1986) before the discovery of inorganic fullerenes (Tenne et al., 1992).

Recently, there has been increasing interest in generating 3D architectures from 2D crystals, i.e., shaped structures that protrude significantly (substantially more than the thickness of the individual or stacked layers) into the out-of-plane direction. Parallel to continued intense work on 0D and 1D polymorphs such as fullerenes and nanotubes (Bai et al., 2020; Zhang et al., 2019), significant efforts have been dedicated to shaping 2D crystals into increasingly complex 3D architectures. While research in this direction benefits from mechanical properties that, not unlike those of paper (Blees et al., 2015), are amenable to bending, folding, crumpling, and cutting, the expansion into the third dimension is driven by the recognition of inherent limitations of planar mono- and few-layer materials. For example, the interaction with light is governed by different selection rules for different orientations of a 2D crystal relative to the incident radiation (Schuller et al., 2013; Wang et al., 2017), which can lead to distinct optoelectronic properties of planar and standing layers. In addition, control over a 3D shape may allow the realization of photonic structures such as resonators or microcavities made of the active 2D material that can further enhance the interaction with light (Deng et al., 2019). Another important area that can benefit from 3D architectures is catalysis. It has long been recognized that the catalytic properties of graphene can be modified by shaping into the third dimension (Wu et al., 2016; Zhang et al., 2016), for instance as a result of an increased surface area but also because the curvature realized in 3D structures can induce enhanced reactivity and generally tune the chemical properties (Agnoli and Granozzi, 2013). Further enhancements can be obtained by integrating different 2D or 2D/0D materials in shaped or crumpled heterostructures that realize electronic modifications such as local charge separation by p–n nanojunctions (Carraro et al., 2015) along with reduced sintering, dispersion of dopants, and exposure of abundant reactive edge sites to reactants in the gas or liquid phase.

Figure 6 illustrates examples of mechanisms used to create 3D structures from 2D or layered crystals. A recent comprehensive review is provided by Zhang et al. (2021). A frequently used approach to induce out-of-plane bending or folding involves supporting the active 2D crystal on a flexible, stimuli-responsive actuator such as a pair of differentially cross-linked epoxy resist layers (e.g., SU8, Figure 6A) whose bending response can be controlled by different solvents (Huang et al., 2020), or integration in a dual-gradient graphene oxide (GO) paper of hydrophilic reduced GO with GO-polydopamine nanoregions that readily adsorb/desorb water molecules in response to environmental humidity, temperature, or light, and thus provide an externally controlled dynamic volume expansion/contraction (Mu et al., 2015) (Figure 6B). While these approaches are reminiscent of macroscopic paper folding (or origami), the variation that involves cutting of paper (kirigami) also inspires 3D architectures of 2D crystals. "Cutting" of graphene using lithographic techniques provides the basis for a number of 3D architectures. The example shown in Figure 6C illustrates a stretchable graphene transistor (Blees et al., 2015). Liquid-gated by an aqueous 10 mM KCl electrolyte, the device showed negligible changes in its transconductance between the native (unstretched) state and stretched to 240% of its intrinsic length. The same authors also demonstrated the ability of remotely actuating pyramidal graphene kirigami springs, e.g., by using the photon pressure of a laser focused on a graphene pad connected to a larger support via several layers of cut graphene hinges.

A different type of 3D architecture involves cylindrical scrolls of 2D crystals or heterostacks. Figure 6D illustrates an approach toward self-rolled cylindrical devices induced by a bimetal-like support (Deng et al., 2019), inspired by scrolls realized with pairs of strained epitaxial 3D-crystalline semiconductor films released from their substrate (Schmidt and Eberl, 2001). In the 2D case, graphene along with patterned contacts, supported on strained SiN_x layer pairs and released by etching of a sacrificial Al film, is rolled up into a cylindrical FET photodetector. A similar fabrication method has been reported for other 2D crystals, including MoS_2 (Deng et al., 2020), while alternative approaches use evaporated bimetallic strips both for rolling and as device contacts (Zhou et al., 2019). The cylindrical graphene FET

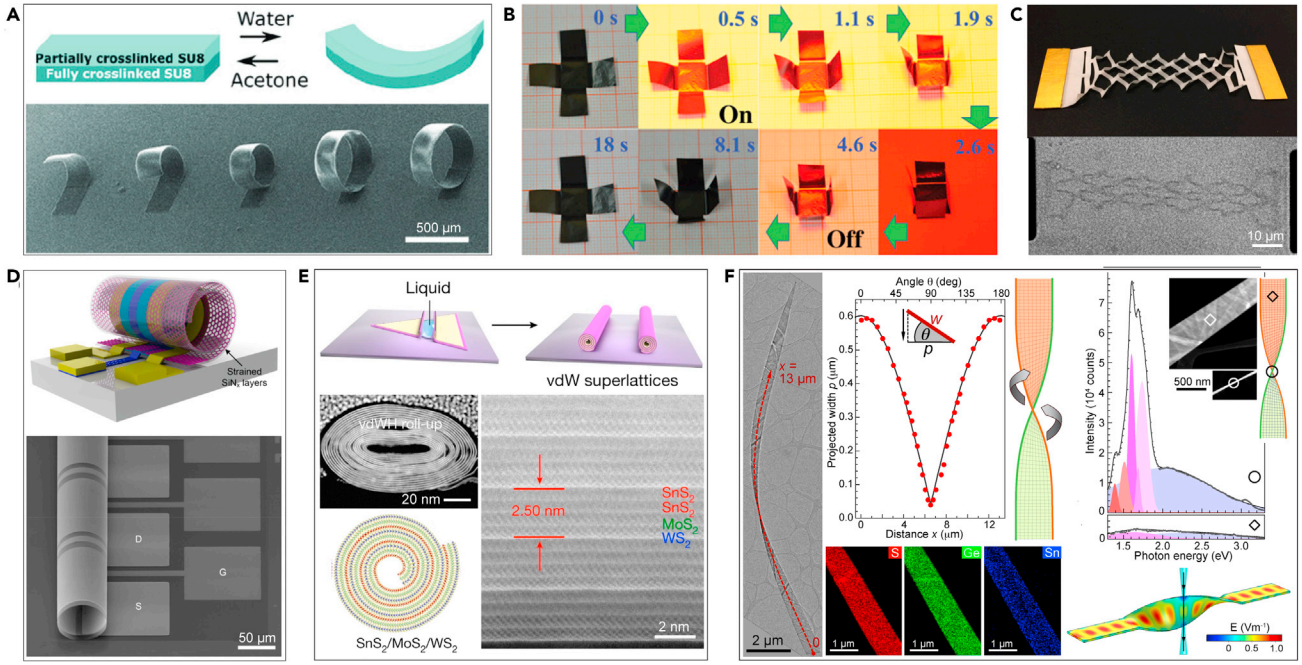

Figure 6. 3D architectures of 2D/layered crystals

(A and B) Shape tuning and self-folding using stimuli-responsive actuators. (A) Solvent-induced self-actuation of graphene membranes using differentially cross-linked films of an SU8 negative epoxy. Adapted from Huang et al. (2020). Copyright 2020 Wiley-VCH. (B) Reversible self-folding of a box made of graphene paper, actuated by near-infrared (NIR) light exposure (On: with NIR light; Off: without NIR light). Adapted from Mu et al. (2015). Copyright 2015 American Association for the Advancement of Science.

(C) Graphene kirigami for stretchable graphene electronics. Top: Paper model; Bottom: Graphene spring stretched by ~70% from its rest length. Adapted from Blees et al. (2015). Copyright 2015 Springer Nature. (D and E) Scrolls of 2D crystals and heterostacks.

(D) Self-rolled-up 3D graphene field-effect transistor (GFET) photodetector, using a combination of compressively strained and tensile strained SiN_x support layers and a sacrificial Al release layer. Adapted from Deng et al. (2019). Copyright 2019 American Chemical Society.

(E) High-order superlattices of van der Waals heterostructures spontaneously generated by delamination via liquid intercalation at the interface to the substrate and a capillary force induced spontaneous rolling process. Adapted from Zhao et al. (2021). Copyright 2021 Springer Nature.

(F) Spontaneous twisting of chalcogenide nanoribbons. $Ge_{1-x}Sn_xS$ alloy nanoribbons with SnS enriched edges, synthesized by Au-catalyzed vapor-liquid-solid growth show spontaneous axial twisting, thus generating 3D waveguides with continuously varying orientation. CL measurements show excitation of traveling TE0 photonic modes by a focused electron beam exclusively in vertical section of the nanoribbon waveguides, where the electrons propagate parallel to the ribbon plane. Adapted from Sutter et al. (2021b). Copyright 2020 Wiley-VCH.

photodetectors demonstrated efficient photodetection in the UV, visible, mid-infrared, and terahertz (THz) regions, while MoS_2 scrolls showed polarization-dependent photocurrent, where symmetry breaking results from the cylindrical geometry of the detector. Generally, it is argued that devices based on 3D scrolls provide enhanced light absorption compared to planar 2D photodetectors. A related approach toward rolled-up 2D crystals is illustrated in Figure 6E. Here, a liquid such as an alcohol-water mixture (Cui et al., 2018) or an ethanol-water-ammonia solution (Zhao et al., 2021) delaminates the 2D crystal from the substrate and induces the spontaneous rolling process, presumably due to capillary forces, i.e., no strained support is needed as an actuator to drive self-rolling. As shown in Figure 6E, vertical van der Waals stacks of different 2D crystals (e.g., $SnS_2/MoS_2/WS_2$) can be rolled into high-order superlattices with multiple repeat periods that would be difficult to produce in planar form using current state-of-the-art technology. In addition, by tuning the rolling direction chiral scrolls can be produced in which the adjacent superlattice periods form a twisted interface (Zhao et al., 2021), thus providing an alternative to the conventional twisted mechanical stacking (Kim et al., 2016), bottom-up synthesis (Sutter et al., 2019c), as well as methods based on Eshelby twist in nanowires (Sutter et al., 2019e) to controllably generate twist moirés at van der Waals interfaces. The liquid-induced formation of curved superlattices has been extended to other combinations of 2D crystals (e.g., $NbSe_2/MoSe_2$), as well as joined 3D and 2D crystal layers (e.g., Al_2O_3/WSe_2), and represents a versatile strategy toward engineering electronic band structure, generating photonic metamaterials, etc.

Nanoribbons have long been recognized for providing opportunities to shape 2D and layered crystals into 3D architectures. Early work has focused on graphene nanoribbons, for which edge-stresses can induce ripples, warping (Shenoy et al., 2008), as well as axial twisting (Ramasubramaniam et al., 2012). The recent evolution of this concept into the realm of chalcogenide semiconductor ribbons is shown in Figure 6F. Forests of ultrathin single-crystalline $Ge_{1-x}Sn_xS$ monochalcogenide alloy nanoribbons are synthesized by Au-catalyzed vapor-liquid-solid growth driven by simultaneous exposure to GeS and SnS precursor vapors (Sutter et al., 2021b). An inhomogeneous alloy composition, specifically SnS-enrichment at the edges (implying that the ribbons are few-layer lateral heterostructures), sets up variations in lattice constants that result in compressive edge stress (see Figure 1B), the driving force for spontaneous axial twisting. Since they can project an ultrathin layered semiconductor with continuously varying orientation relative to an exciting electron beam, twisted nanoribbons provide unique opportunities for exciting and probing nanophotonic waveguide modes by CL (Figure 6F). CL spectra obtained in horizontal and vertical sections of twisted $Ge_{1-x}Sn_xS$ ribbons show fundamentally different characteristics. In particular, an intense, sharp band-edge emission peak is excited by the electron beam traveling within the ribbon plane, whereas weak broad-band light emission results from electron trajectories perpendicular to the layered ribbons (Sutter et al., 2021b). These differences cannot be explained simply by different excitation volumes (García de Abajo, 2010); instead, simulations for ultrathin twisted ribbons show that in-plane passage of the high-energy electron beam (in a vertical ribbon section) excites propagating transverse electric (TE_0) waveguide modes with electric field parallel to the beam trajectory, whereas perpendicular passage (in planar ribbon sections) only generates weak, localized fields. Intermediate orientations of the ribbons relative to the exciting electron beam produce weaker waveguide mode emission whose intensity scales with the local tilt angle, θ. In thicker ribbons or flakes hosting higher-order photonic modes, the constraints identified in ultrathin ribbons are relaxed and electron beams incident perpendicular to the ribbon/flake plane are also capable of exciting propagating modes (Sutter et al., 2018). A similar electron-beam launching of long-range propagating modes in van der Waals nanoribbon waveguides has been observed for (straight) GaSe ribbons obtained by vapor-liquid-solid growth (Sutter et al., 2021a). These combined findings point to interesting future directions, where van der Waals nanoribbons twisted into the third dimension could serve as platforms for probing energy and information transfer or coupling mechanisms, e.g., in support of quantum information science. For example, embedded quantum nodes or single photon emitters, already identified for a number of 2D/layered semiconductors including WSe_2 (Chakraborty et al., 2015; He et al., 2015; Koperski et al., 2015; Srivastava et al., 2015), h-BN (Tran et al., 2016), and GaSe (Tonndorf et al., 2017), and controllably induced by elastic strain (Kern et al., 2016; Palacios-Berraquero et al., 2017), can be combined with ultrathin waveguides to study photonic information transfer using electron beam excitation and CL detection.

CONCLUSIONS

Clearly, one can envision van der Waals architectures with a diversity that goes far beyond the well-known vertical stacks and 2D in-plane bonded lateral heterostructures once a minimal set of prerequisites is met. Perhaps most important is the readiness to think beyond the concept of a planar monolayer, and either venture into the realm of few-layer and multilayer van der Waals crystals or, as discussed in the last section of this perspective, explore ways to controllably bring 2D crystals into the third dimension. None of the heterostructures highlighted here are accessible through exfoliation and stacking, which points to the crucial importance of developing synthesis and post-growth processing for creating novel heterostructures with complex interface geometries. In situ microscopy, performed under often challenging growth and processing conditions, should play an increasingly important role in understanding the microscopic mechanisms involved in the generation of unconventional heterostructures and quantifying the relevant thermodynamic and kinetic factors.

The formation of van der Waals heterostructures through phase conversion requires materials with multiple stable or metastable polymorphs as found among some of the TMDs, or several stable layered bulk phases as realized in the tin chalcogenides. The latter lend themselves exceptionally well to the exploration of unconventional van der Waals architectures since a simple tuning of the chalcogen chemical potential, e.g., by using different precursors or controlling the partial pressure of S or Se, allows the facile transitioning between different non-isotypic layered crystals. The question then arises if such an intrinsic tunability can be found in other classes of 2D/layered crystals. Among the known candidates are some of the early transition metal chalcogenides. For example, layered Zr, Ta, and Hf compounds are known to exist in at least two stoichiometries, namely 2D dichalcogenides (MX_2) (Law and Lee, 2017; Zhang et al., 2015) and quasi-1D trichalcogenides (MX_3) (Jin et al., 2011; Mayorga-Martinez et al., 2018; Perluzzo et al., 1980).

Clearly, integrating or interconverting these phases could yield structural conflicts that may result in unexpected architectures, as well as interesting interface-driven functionality.

Whereas heterostructures generated by phase conversion may remain limited to a handful of materials, the concept of using phase separation between structurally incompatible layered crystals to induce spontaneous heterostructure formation could in principle be applied broadly. Here, we highlighted a growth approach in which orthorhombic SnS and trigonal SnS_2 were concurrently (or sequentially) crystallized during vapor transport of SnS with a slight excess of S, thus taking advantage of the structural diversity of the tin chalcogenides to generate wrap-around core-shell heterostructures of layered crystals via phase separation. Similar phase separation processes should take place during the co-crystallization of a wide variety of other layered materials with different crystal structures. The primary challenge in realizing diverse heterostructures using this approach will be to avoid alloying between the different components, which occurs readily among transition metal (Mo, W) dichalcogenides (Huang et al., 2014b). Note that the issue of alloying does not arise if the two competing crystal phases only differ in their chalcogen content, as has been the case for the group IV chalcogenides (Sutter et al., 2019b, 2019d). Ge and Sn monochalcogenides bring to bear additional advantages in few-layer and multilayer heterostructures. In contrast to the TMDs, which beyond the initial monolayer tend to grow as pyramidal stacks with gradually shrinking layer footprint (Zheng et al., 2017), few-layer and multilayer SnS and GeS flakes crystallize with (001) top/bottom and {110} side facets, i.e., their sides are perfectly vertical to the substrate plane so that they can form compact seeds for unconventional heterostructures (Sutter et al., 2019a, 2019b).

The relatively recent research direction aiming to shape 2D/layered crystals into 3D architectures, finally, has great potential for creating functional materials tailored for device applications, for example integrated optoelectronic and photonic systems. Along with wrap-around heterostructures that host different interface geometries, folded, rolled, or twisted van der Waals crystals pose particular challenges in probing light-matter interactions near interfaces. Whereas near-field optical methods are well suited for interrogating planar structures, electron beam methods such as CL and EELS readily accommodate thicker heterostructures that protrude significantly into the third dimension. Hence, it is likely that further progress in 3D architectures from 2D crystals will be accompanied by increasing application and further development of (S)TEM based spectroscopies for probing optoelectronic and photonic properties at local (nanometer) scales.

Limitations of the study

Not applicable for perspectives paper.

ACKNOWLEDGMENTS

This work was supported by the U.S. Department of Energy, Office of Science, Basic Energy Sciences under Award No. DE-SC0016343.

AUTHOR CONTRIBUTIONS

P.S. and E.S. co-wrote this perspective.

DECLARATION OF INTERESTS

The authors declare no competing interests.

REFERENCES

Agnoli, S., and Granozzi, G. (2013). Second generation graphene: opportunities and challenges for surface science. Surf. Sci. *609*, 1–5. https://doi.org/10.1016/j.susc.2012.11.016.

Ahn, S.J., Moon, P., Kim, T.-H., Kim, H.-W., Shin, H.-C., Kim, E.H., Cha, H.W., Kahng, S.-J., Kim, P., Koshino, M., et al. (2018). Dirac electrons in a dodecagonal graphene quasicrystal. Science *361*, 782–786. https://doi.org/10.1126/science.aar8412.

Bai, Y., Yue, H., Wang, J., Shen, B., Sun, S., Wang, S., Wang, H., Li, X., Xu, Z., Zhang, R., and Wei, F. (2020). Super-durable ultralong carbon nanotubes. Science *369*, 1104–1106. https://doi.org/10.1126/science.aay5220.

Bao, W., Borys, N.J., Ko, C., Suh, J., Fan, W., Thron, A., Zhang, Y., Buyanin, A., Zhang, J., Cabrini, S., et al. (2015). Visualizing nanoscale excitonic relaxation properties of disordered edges and grain boundaries in monolayer molybdenum disulfide. Nat. Commun. *6*, 7993. https://doi.org/10.1038/ncomms8993.

Bao, W., Melli, M., Caselli, N., Riboli, F., Wiersma, D.S., Staffaroni, M., Choo, H., Ogletree, D.F., Aloni, S., Bokor, J., et al. (2012). Mapping local charge recombination heterogeneity by multidimensional nanospectroscopic imaging. Science *338*, 1317–1321. https://doi.org/10.1126/science.1227977.

Bauer, E. (2020). Surface microscopy with low energy electrons: LEEM. J. Electron Spectrosc. Relat. Phenomena *241*, 146806. https://doi.org/10.1016/j.elspec.2018.11.005.

Blees, M.K., Barnard, A.W., Rose, P.A., Roberts, S.P., McGill, K.L., Huang, P.Y., Ruyack, A.R., Kevek, J.W., Kobrin, B., Muller, D.A., and

McEuen, P.L. (2015). Graphene kirigami. Nature *524*, 204–207. https://doi.org/10.1038/nature14588.

Burton, L.A., Whittles, T.J., Hesp, D., Linhart, W.M., Skelton, J.M., Hou, B., Webster, R.F., O'Dowd, G., Reece, C., Cherns, D., et al. (2016). Electronic and optical properties of single crystal SnS_2: an earth-abundant disulfide photocatalyst. J. Mater. Chem. A *4*, 1312–1318. https://doi.org/10.1039/C5TA08214E.

Cadiz, F., Robert, C., Courtade, E., Manca, M., Martinelli, L., Taniguchi, T., Watanabe, K., Amand, T., Rowe, A.C.H., Paget, D., et al. (2018). Exciton diffusion in WSe_2 monolayers embedded in a van der Waals heterostructure. Appl. Phys. Lett. *112*, 152106. https://doi.org/10.1063/1.5026478.

Cao, Y., Fatemi, V., Fang, S., Watanabe, K., Taniguchi, T., Kaxiras, E., and Jarillo-Herrero, P. (2018). Unconventional superconductivity in magic-angle graphene superlattices. Nature *556*, 43–50. https://doi.org/10.1038/nature26160.

Carraro, F., Calvillo, L., Cattelan, M., Favaro, M., Righetto, M., Nappini, S., Píš, I., Celorrio, V., Fermín, D.J., Martucci, A., et al. (2015). Fast one-pot synthesis of MoS_2/crumpled graphene p–n nanonjunctions for enhanced photoelectrochemical hydrogen production. ACS Appl. Mater. Interfaces *7*, 25685–25692. https://doi.org/10.1021/acsami.5b06668.

Chakraborty, C., Kinnischtzke, L., Goodfellow, K.M., Beams, R., and Vamivakas, A.N. (2015). Voltage-controlled quantum light from an atomically thin semiconductor. Nat. Nanotechnol. *10*, 507–511. https://doi.org/10.1038/nnano.2015.79.

Chung, W.F., and Altman, M.S. (1998). Step contrast in low energy electron microscopy. Ultramicroscopy *74*, 237–246. https://doi.org/10.1016/S0304-3991(98)00043-6.

Cui, X., Kong, Z., Gao, E., Huang, D., Hao, Y., Shen, H., Di, C.-a., Xu, Z., Zheng, J., and Zhu, D. (2018). Rolling up transition metal dichalcogenide nanoscrolls via one drop of ethanol. Nat. Commun. *9*, 1301. https://doi.org/10.1038/s41467-018-03752-5.

Dai, S., Quan, J., Hu, G., Qiu, C.-W., Tao, T.H., Li, X., and Alù, A. (2019). Hyperbolic phonon polaritons in suspended hexagonal boron nitride. Nano Lett. *19*, 1009–1014. https://doi.org/10.1021/acs.nanolett.8b04242.

Deng, T., Li, S., Li, Y., Zhang, Y., Sun, J., Yin, W., Wu, W., Zhu, M., Wang, Y., and Liu, Z. (2020). Polarization-sensitive photodetectors based on three-dimensional molybdenum disulfide (MoS_2) field-effect transistors. Nanophotonics *9*, 4719–4728. https://doi.org/10.1515/nanoph-2020-0401.

Deng, T., Zhang, Z., Liu, Y., Wang, Y., Su, F., Li, S., Zhang, Y., Li, H., Chen, H., Zhao, Z., et al. (2019). Three-dimensional graphene field-effect transistors as high-performance photodetectors. Nano Lett. *19*, 1494–1503. https://doi.org/10.1021/acs.nanolett.8b04099.

Duan, X., Wang, C., Shaw, J.C., Cheng, R., Chen, Y., Li, H., Wu, X., Tang, Y., Zhang, Q., Pan, A., et al. (2014). Lateral epitaxial growth of two-dimensional layered semiconductor heterojunctions. Nat. Nanotechnol. *9*, 1024–1030. https://doi.org/10.1038/nnano.2014.222.

Eda, G., Fujita, T., Yamaguchi, H., Voiry, D., Chen, M., and Chhowalla, M. (2012). Coherent atomic and electronic heterostructures of single-layer MoS_2. ACS Nano *6*, 7311–7317. https://doi.org/10.1021/nn302422x.

Faist, J., Capasso, F., Sivco, D.L., Sirtori, C., Hutchinson, A.L., and Cho, A.Y. (1994). Quantum cascade laser. Science *264*, 553–556. https://doi.org/10.1126/science.264.5158.553.

Fei, R., Kang, W., and Yang, L. (2016). Ferroelectricity and phase transitions in monolayer group-IV monochalcogenides. Phys. Rev. Lett. *117*, 097601. https://doi.org/10.1103/PhysRevLett.117.097601.

Fei, R., Li, W., Li, J., and Yang, L. (2015). Giant piezoelectricity of monolayer group IV monochalcogenides: SnSe, SnS, GeSe, and GeS. Appl. Phys. Lett. *107*, 173104. https://doi.org/10.1063/1.4934750.

Frisenda, R., Navarro-Moratalla, E., Gant, P., Pérez De Lara, D., Jarillo-Herrero, P., Gorbachev, R.V., and Castellanos-Gomez, A. (2018). Recent progress in the assembly of nanodevices and van der Waals heterostructures by deterministic placement of 2D materials. Chem. Soc. Rev. *47*, 53–68. https://doi.org/10.1039/C7CS00556C.

Funke, S., Miller, B., Parzinger, E., Thiesen, P., Holleitner, A.W., and Wurstbauer, U. (2016). Imaging spectroscopic ellipsometry of MoS_2. J. Phys. Condensed Matter *28*, 385301. https://doi.org/10.1088/0953-8984/28/38/385301.

Gao, P., Wang, L., Zhang, Y.-Y., Huang, Y., Liao, L., Sutter, P., Liu, K., Yu, D., and Wang, E.-G. (2016). High-resolution tracking asymmetric lithium insertion and extraction and local structure ordering in SnS_2. Nano Lett. *16*, 5582–5588. https://doi.org/10.1021/acs.nanolett.6b02136.

García de Abajo, F.J. (2010). Optical excitations in electron microscopy. Rev. Mod. Phys. *82*, 209–275. https://doi.org/10.1103/RevModPhys.82.209.

Geim, A.K., and Grigorieva, I.V. (2013). Van der Waals heterostructures. Nature *499*, 419–425. https://doi.org/10.1038/nature12385.

Gogoi, P.K., Lin, Y.-C., Senga, R., Komsa, H.-P., Wong, S.L., Chi, D., Krasheninnikov, A.V., Li, L.-J., Breese, M.B.H., Pennycook, S.J., et al. (2019). Layer rotation-angle-dependent excitonic absorption in van der Waals heterostructures revealed by electron energy loss spectroscopy. ACS Nano *13*, 9541–9550. https://doi.org/10.1021/acsnano.9b04530.

Gomes, L.C., and Carvalho, A. (2015). Phosphorene analogues: isoelectronic two-dimensional group-IV monochalcogenides with orthorhombic structure. Phys. Rev. B *92*, 085406. https://doi.org/10.1103/PhysRevB.92.085406.

Gong, Y., Lin, J., Wang, X., Shi, G., Lei, S., Lin, Z., Zou, X., Ye, G., Vajtai, R., Yakobson, B.I., et al. (2014). Vertical and in-plane heterostructures from WS_2/MoS_2 monolayers. Nat. Mater. *13*, 1135–1142. https://doi.org/10.1038/nmat4091.

Greyson, E.C., Barton, J.E., and Odom, T.W. (2006). Tetrahedral zincblende tin sulfide nano- and microcrystals. Small *2*, 368–371. https://doi.org/10.1002/smll.200500460.

Havener, R.W., Kim, C.-J., Brown, L., Kevek, J.W., Sleppy, J.D., McEuen, P.L., and Park, J. (2013). Hyperspectral imaging of structure and composition in atomically thin heterostructures. Nano Lett. *13*, 3942–3946. https://doi.org/10.1021/nl402062j.

He, Y.-M., Clark, G., Schaibley, J.R., He, Y., Chen, M.-C., Wei, Y.-J., Ding, X., Zhang, Q., Yao, W., Xu, X., et al. (2015). Single quantum emitters in monolayer semiconductors. Nat. Nanotechnol. *10*, 497–502. https://doi.org/10.1038/nnano.2015.75.

Higashitarumizu, N., Kawamoto, H., Lee, C.-J., Lin, B.-H., Chu, F.-H., Yonemori, I., Nishimura, T., Wakabayashi, K., Chang, W.-H., and Nagashio, K. (2020). Purely in-plane ferroelectricity in monolayer SnS at room temperature. Nat. Commun. *11*, 2428. https://doi.org/10.1038/s41467-020-16291-9.

Ho, C.-H., Lee, H.-W., and Cheng, Z.-H. (2004). Practical thermoreflectance design for optical characterization of layer semiconductors. Rev. Sci. Instr. *75*, 1098–1102. https://doi.org/10.1063/1.1667255.

Hong, J., Senga, R., Pichler, T., and Suenaga, K. (2020). Probing exciton dispersions of freestanding monolayer WSe_2 by momentum-resolved electron energy-loss spectroscopy. Phys. Rev. Lett. *124*, 087401. https://doi.org/10.1103/PhysRevLett.124.087401.

Hu, F., Luan, Y., Scott, M.E., Yan, J., Mandrus, D.G., Xu, X., and Fei, Z. (2017). Imaging exciton–polariton transport in $MoSe_2$ waveguides. Nat. Photon. *11*, 356–360. https://doi.org/10.1038/nphoton.2017.65.

Huang, C.-C., Lin, Y.-J., Chuang, C.-Y., Liu, C.-J., and Yang, Y.-W. (2013). Conduction-type control of SnS_x films prepared by the sol–gel method for different sulfur contents. J. Alloys Compd. *553*, 208–211. https://doi.org/10.1016/j.jallcom.2012.11.134.

Huang, Q., Deng, T., Xu, W., Yoon, C., Qin, Z., Lin, Y., Li, T., Yang, Y., Shen, M., Thon, S.M., et al. (2020). Solvent responsive self-folding of 3D photosensitive graphene architectures. Adv. Intell. Syst. 2000195. https://doi.org/10.1002/aisy.202000195.

Huang, Y., Sutter, E., Wu, L.M., Xu, H., Bao, L., Gao, H.-J., Zhou, X.-J., and Sutter, P. (2018). Thick layered semiconductor devices with water top-gates: high on–off ratio field-effect transistors and aqueous sensors. ACS Appl. Mater. Interfaces *10*, 23198–23207. https://doi.org/10.1021/acsami.8b05932.

Huang, C., Wu, S., Sanchez, A.M., Peters, J.J.P., Beanland, R., Ross, J.S., Rivera, P., Yao, W., Cobden, D.H., and Xu, X. (2014b). Lateral heterojunctions within monolayer $MoSe_2$–WSe_2 semiconductors. Nat. Mater. *13*, 1096–1101. https://doi.org/10.1038/nmat4064.

Huang, Y., Sutter, E., Sadowski, J.T., Cotlet, M., Monti, O.L.A., Racke, D.A., Neupane, M.R., Wickramaratne, D., Lake, R.K., Parkinson, B.A., and Sutter, P. (2014a). Tin disulfide—an emerging

layered metal dichalcogenide semiconductor: materials properties and device characteristics. ACS Nano *8*, 10743–10755. https://doi.org/10.1021/nn504481r.

Huang, Y., Sutter, E., Shi, N.N., Zheng, J., Yang, T., Englund, D., Gao, H.-J., and Sutter, P. (2015). Reliable exfoliation of large-area high-quality flakes of graphene and other two-dimensional materials. ACS Nano *9*, 10612–10620. https://doi.org/10.1021/acsnano.5b04258.

Huang, Y., Zang, H., Chen, J.-S., Sutter, E.A., Sutter, P.W., Nam, C.-Y., and Cotlet, M. (2016). Hybrid quantum dot-tin disulfide field-effect transistors with improved photocurrent and spectral responsivity. Appl. Phys. Lett. *108*, 123502. https://doi.org/10.1063/1.4944781.

Ichimura, M., Takeuchi, K., Ono, Y., and Arai, E. (2000). Electrochemical deposition of SnS thin films. Thin Solid Films *361-362*, 98–101. https://doi.org/10.1016/S0040-6090(99)00798-1.

Iijima, S. (1991). Helical microtubules of graphitic carbon. Nature *354*, 56–58. https://doi.org/10.1038/354056a0.

Jain, A., Ong, S.P., Hautier, G., Chen, W., Richards, W.D., Dacek, S., Cholia, S., Gunter, D., Skinner, D., Ceder, G., and Persson, K.A. (2013). Commentary: the Materials Project: a materials genome approach to accelerating materials innovation. APL Mater. *1*, 011002. https://doi.org/10.1063/1.4812323.

Jin, C., Regan, E.C., Yan, A., Iqbal Bakti Utama, M., Wang, D., Zhao, S., Qin, Y., Yang, S., Zheng, Z., Shi, S., et al. (2019). Observation of moiré excitons in WSe_2/WS_2 heterostructure superlattices. Nature *567*, 76–80. https://doi.org/10.1038/s41586-019-0976-y.

Jin, H., Cheng, D., Li, J., Cao, X., Li, B., Wang, X., Liu, X., and Zhao, X. (2011). Facile synthesis of zirconium trisulfide and hafnium trisulfide nanobelts: growth mechanism and Raman spectroscopy. Solid State Sci. *13*, 1166–1171. https://doi.org/10.1016/j.solidstatesciences.2010.12.017.

Joensen, P., Frindt, R.F., and Morrison, S.R. (1986). Single-layer MoS_2. Mater. Res. Bull. *21*, 457–461. https://doi.org/10.1016/0025-5408(86)90011-5.

Julien, C., Eddrief, M., Samaras, I., and Balkanski, M. (1992). Optical and electrical characterizations of SnSe, SnS_2 and $SnSe_2$ single crystals. Mater. Sci. Eng. B *15*, 70–72. https://doi.org/10.1016/0921-5107(92)90033-6.

Kappera, R., Voiry, D., Yalcin, S.E., Branch, B., Gupta, G., Mohite, A.D., and Chhowalla, M. (2014). Phase-engineered low-resistance contacts for ultrathin MoS_2 transistors. Nat. Mater. *13*, 1128–1134. https://doi.org/10.1038/nmat4080.

Kern, J., Niehues, I., Tonndorf, P., Schmidt, R., Wigger, D., Schneider, R., Stiehm, T., Michaelis de Vasconcellos, S., Reiter, D.E., Kuhn, T., and Bratschitsch, R. (2016). Nanoscale positioning of single-photon emitters in atomically thin WSe_2. Adv. Mater. *28*, 7101–7105. https://doi.org/10.1002/adma.201600560.

Kim, K., Yankowitz, M., Fallahazad, B., Kang, S., Movva, H.C.P., Huang, S., Larentis, S., Corbet, C.M., Taniguchi, T., Watanabe, K., et al. (2016). Van der Waals heterostructures with high accuracy rotational alignment. Nano Lett. *16*, 1989–1995. https://doi.org/10.1021/acs.nanolett.5b05263.

Kim, J.H., Yun, S.J., Lee, H.S., Zhao, J., Bouzid, H., and Lee, Y.H. (2018a). Plasma-induced phase transformation of SnS_2 to SnS. Sci. Rep. *8*, 10284. https://doi.org/10.1038/s41598-018-28323-y.

Kim, Y.C., Nguyen, V.T., Lee, S., Park, J.-Y., and Ahn, Y.H. (2018b). Evaluation of transport parameters in MoS_2/graphene junction devices fabricated by chemical vapor deposition. ACS Appl. Mater. Interfaces *10*, 5771–5778. https://doi.org/10.1021/acsami.7b16177.

Kim, Y., Hwang, H., Lawler, K., Martin, S.W., and Cho, J. (2008). Electrochemical behavior of Ge and GeX_2 (X = O, S) glasses: improved reversibility of the reaction of Li with Ge in a sulfide medium. Electrochim. Acta *53*, 5058–5064. https://doi.org/10.1016/j.electacta.2007.12.015.

Koperski, M., Nogajewski, K., Arora, A., Cherkez, V., Mallet, P., Veuillen, J.Y., Marcus, J., Kossacki, P., and Potemski, M. (2015). Single photon emitters in exfoliated WSe_2 structures. Nat. Nanotechnol. *10*, 503–506. https://doi.org/10.1038/nnano.2015.67.

Krivanek, O.L., Lovejoy, T.C., Dellby, N., Aoki, T., Carpenter, R.W., Rez, P., Soignard, E., Zhu, J., Batson, P.E., Lagos, M.J., et al. (2014). Vibrational spectroscopy in the electron microscope. Nature *514*, 209–212. https://doi.org/10.1038/nature13870.

Kroto, H.W., Heath, J.R., O'Brien, S.C., Curl, R.F., and Smalley, R.E. (1985). C60: buckminsterfullerene. Nature *318*, 162–163. https://doi.org/10.1038/318162a0.

Law, K.T., and Lee, P.A. (2017). 1T-TaS_2 as a quantum spin liquid. Proc. Natl. Acad. Sci. U S A *114*, 6996–7000. https://doi.org/10.1073/pnas.1706769114.

Levendorf, M.P., Kim, C.-J., Brown, L., Huang, P.Y., Havener, R.W., Muller, D.A., and Park, J. (2012). Graphene and boron nitride lateral heterostructures for atomically thin circuitry. Nature *488*, 627–632. https://doi.org/10.1038/nature11408.

Li, M.-Y., Shi, Y., Cheng, C.-C., Lu, L.-S., Lin, Y.-C., Tang, H.-L., Tsai, M.-L., Chu, C.-W., Wei, K.-H., He, J.-H., et al. (2015). Epitaxial growth of a monolayer WSe_2–MoS_2 lateral p–n junction with an atomically sharp interface. Science *349*, 524–528. https://doi.org/10.1126/science.aab4097.

Lin, S., Carvalho, A., Yan, S., Li, R., Kim, S., Rodin, A., Carvalho, L., Chan, E.M., Wang, X., Castro Neto, A.H., and Yao, J. (2018). Accessing valley degree of freedom in bulk tin(II) sulfide at room temperature. Nat. Commun. *9*, 1455. https://doi.org/10.1038/s41467-018-03897-3.

Lin, Y.-C., Dumcenco, D.O., Huang, Y.-S., and Suenaga, K. (2014). Atomic mechanism of the semiconducting-to-metallic phase transition in single-layered MoS_2. Nat. Nanotechnol. *9*, 391–396. https://doi.org/10.1038/nnano.2014.64.

Liu, Y., Weiss, N.O., Duan, X., Cheng, H.-C., Huang, Y., and Duan, X. (2016). Van der Waals heterostructures and devices. Nat. Rev. Mater. *1*, 16042. https://doi.org/10.1038/natrevmats.2016.42.

Mariano, A.N., and Chopra, K.L. (1967). Polymorphism in some IV–VI compounds induced by high pressure and thin film epitaxial growth. Appl. Phys. Lett. *10*, 282–284. https://doi.org/10.1063/1.1754812.

Mayorga-Martinez, C.C., Sofer, Z., Luxa, J., Huber, Š., Sedmidubský, D., Brázda, P., Palatinus, L., Mikulics, M., Lazar, P., Medlín, R., and Pumera, M. (2018). TaS_3 nanofibers: layered trichalcogenide for high-performance electronic and sensing devices. ACS Nano *12*, 464–473. https://doi.org/10.1021/acsnano.7b06853.

Mu, J., Hou, C., Wang, H., Li, Y., Zhang, Q., and Zhu, M. (2015). Origami-inspired active graphene-based paper for programmable instant self-folding walking devices. Sci. Adv. *1*, e1500533. https://doi.org/10.1126/sciadv.1500533.

Nakamura, S., Senoh, M., Nagahama, S.-i., Iwasa, N., Yamada, T., Matsushita, T., Sugimoto, Y., and Kiyoku, H. (1997). Subband emissions of InGaN multi-quantum-well laser diodes under room-temperature continuous wave operation. Appl. Phys. Lett. *70*, 2753–2755. https://doi.org/10.1063/1.118973.

Nazin, G., Zhang, Y., Zhang, L., Sutter, E., and Sutter, P. (2010). Visualization of charge transport through Landau levels in graphene. Nat. Phys. *6*, 870–874. https://doi.org/10.1038/nphys1745.

Ni, G.X., McLeod, A.S., Sun, Z., Wang, L., Xiong, L., Post, K.W., Sunku, S.S., Jiang, B.Y., Hone, J., Dean, C.R., et al. (2018). Fundamental limits to graphene plasmonics. Nature *557*, 530–533. https://doi.org/10.1038/s41586-018-0136-9.

Novoselov, K.S., Geim, A.K., Morozov, S.V., Jiang, D., Zhang, Y., Dubonos, S.V., Grigorieva, I.V., and Firsov, A.A. (2004). Electric field effect in atomically thin carbon films. Science *306*, 666–669. https://doi.org/10.1126/science.1102896.

Novoselov, K.S., Mishchenko, A., Carvalho, A., and Castro Neto, A.H. (2016). 2D materials and van der Waals heterostructures. Science *353*, aac9439. https://doi.org/10.1126/science.aac9439.

Ohtomo, A., and Hwang, H.Y. (2004). A high-mobility electron gas at the $LaAlO_3/SrTiO_3$ heterointerface. Nature *427*, 423–426. https://doi.org/10.1038/nature02308.

Palacios-Berraquero, C., Kara, D.M., Montblanch, A.R.P., Barbone, M., Latawiec, P., Yoon, D., Ott, A.K., Loncar, M., Ferrari, A.C., and Atatüre, M. (2017). Large-scale quantum-emitter arrays in atomically thin semiconductors. Nat. Commun. *8*, 15093. https://doi.org/10.1038/ncomms15093.

Parenteau, M., and Carlone, C. (1990). Influence of temperature and pressure on the electronic transitions in SnS and SnSe semiconductors. Phys. Rev. B *41*, 5227–5234. https://doi.org/10.1103/PhysRevB.41.5227.

Perluzzo, G., Lakhani, A.A., and Jandl, S. (1980). Electrical transport measurements in a quasi-onedimensional semiconductor ZrS_3. Solid State Commun. *35*, 301–304. https://doi.org/10.1016/0038-1098(80)90503-7.

Phillips, J.C. (1979). Topology of covalent non-crystalline solids I: short-range order in chalcogenide alloys. J. Non-Cryst. Sol. *34*, 153–181. https://doi.org/10.1016/0022-3093(79)90033-4.

Py, M.A., and Haering, R.R. (1983). Structural destabilization induced by lithium intercalation in MoS_2 and related compounds. Can. J. Phys. *61*, 76–84. https://doi.org/10.1139/p83-013.

Rabkin, A., Samuha, S., Abutbul, R.E., Ezersky, V., Meshi, L., and Golan, Y. (2015). New nanocrystalline materials: a previously unknown simple cubic phase in the SnS binary system. Nano Lett. *15*, 2174–2179. https://doi.org/10.1021/acs.nanolett.5b00209.

Ramasubramaniam, A., Koskinen, P., Kit, O.O., and Shenoy, V.B. (2012). Edge-stress-induced spontaneous twisting of graphene nanoribbons. J. Appl. Phys. *111*, 054302. https://doi.org/10.1063/1.3689814.

Reyren, N., Thiel, S., Caviglia, A.D., Kourkoutis, L.F., Hammerl, G., Richter, C., Schneider, C.W., Kopp, T., Rüetschi, A.-S., Jaccard, D., et al. (2007). Superconducting interfaces between insulating oxides. Science *317*, 1196–1199. https://doi.org/10.1126/science.1146006.

Ristov, M., Sinadinovski, G., Grozdanov, I., and Mitreski, M. (1989). Chemical deposition of tin(II) sulphide thin films. Thin Solid Films *173*, 53–58. https://doi.org/10.1016/0040-6090(89)90536-1.

Rochow, E.G., and Abel, E.W. (1973). The chemistry of germanium, tin, and lead (Pergamon Press).

Sanchez-Juarez, A., and Ortiz, A. (2002). Effects of precursor concentration on the optical and electrical properties of Sn_xS_y thin films prepared by plasma-enhanced chemical vapour deposition. Semicond. Sci. Technol. *17*, 931–937. https://doi.org/10.1088/0268-1242/17/9/305.

Sang, X., Li, X., Zhao, W., Dong, J., Rouleau, C.M., Geohegan, D.B., Ding, F., Xiao, K., and Unocic, R.R. (2018). In situ edge engineering in two-dimensional transition metal dichalcogenides. Nat. Commun. *9*, 2051. https://doi.org/10.1038/s41467-018-04435-x.

Schmidt, O.G., and Eberl, K. (2001). Thin solid films roll up into nanotubes. Nature *410*, 168. https://doi.org/10.1038/35065525.

Schuller, J.A., Karaveli, S., Schiros, T., He, K., Yang, S., Kymissis, I., Shan, J., and Zia, R. (2013). Orientation of luminescent excitons in layered nanomaterials. Nat. Nanotechnol. *8*, 271–276. https://doi.org/10.1038/nnano.2013.20.

Seyler, K.L., Rivera, P., Yu, H., Wilson, N.P., Ray, E.L., Mandrus, D.G., Yan, J., Yao, W., and Xu, X. (2019). Signatures of moiré-trapped valley excitons in $MoSe_2/WSe_2$ heterobilayers. Nature *567*, 66–70. https://doi.org/10.1038/s41586-019-0957-1.

Shabani, S., Halbertal, D., Wu, W., Chen, M., Liu, S., Hone, J., Yao, W., Basov, D.N., Zhu, X., and Pasupathy, A.N. (2021). Deep moiré potentials in twisted transition metal dichalcogenide bilayers. Nat. Phys. *17*, 720–725. https://doi.org/10.1038/s41567-021-01174-7.

Sharma, R.C., and Chang, Y.A. (1986). The Se–Sn (selenium–tin) system. Bull. Alloy Phase Diagr. *7*, 68–72. https://doi.org/10.1007/BF02874984.

Shenoy, V.B., Reddy, C.D., Ramasubramaniam, A., and Zhang, Y.W. (2008). Edge-stress-induced warping of graphene sheets and nanoribbons. Phys. Rev. Lett. *101*, 245501. https://doi.org/10.1103/PhysRevLett.101.245501.

Song, H.S., Li, S.L., Gao, L., Xu, Y., Ueno, K., Tang, J., Cheng, Y.B., and Tsukagoshi, K. (2013). High-performance top-gated monolayer SnS_2 field-effect transistors and their integrated logic circuits. Nanoscale *5*, 9666–9670. https://doi.org/10.1039/C3NR01899G.

Splendiani, A., Sun, L., Zhang, Y., Li, T., Kim, J., Chim, C.-Y., Galli, G., and Wang, F. (2010). Emerging photoluminescence in monolayer MoS_2. Nano Lett. *10*, 1271–1275. https://doi.org/10.1021/nl903868w.

Srivastava, A., Sidler, M., Allain, A.V., Lembke, D.S., Kis, A., and Imamoğlu, A. (2015). Optically active quantum dots in monolayer WSe_2. Nat. Nanotechnol. *10*, 491–496. https://doi.org/10.1038/nnano.2015.60.

Stampfli, P. (1986). A dodecagonal quasiperiodic lattice in two dimensions. Helv. Phys. Acta *59*, 1260–1263.

Su, G., Hadjiev, V.G., Loya, P.E., Zhang, J., Lei, S., Maharjan, S., Dong, P.M., Ajayan, P., Lou, J., and Peng, H. (2015). Chemical vapor deposition of thin crystals of layered semiconductor SnS_2 for fast photodetection application. Nano Lett. *15*, 506–513. https://doi.org/10.1021/nl503857r.

Sun, Y., Cheng, H., Gao, S., Sun, Z., Liu, Q., Liu, Q., Lei, F., Yao, T., He, J., Wei, S., and Xie, Y. (2012). Freestanding tin disulfide single-layers realizing efficient visible-light water splitting. Angew. Chem. Int. Ed. *51*, 8727–8731. https://doi.org/10.1002/anie.201204675.

Sunku, S.S., Ni, G.X., Jiang, B.Y., Yoo, H., Sternbach, A., McLeod, A.S., Stauber, T., Xiong, L., Taniguchi, T., Watanabe, K., et al. (2018). Photonic crystals for nano-light in moiré graphene superlattices. Science *362*, 1153–1156. https://doi.org/10.1126/science.aau5144.

Sutter, E., Huang, Y., Komsa, H.P., Ghorbani-Asl, M., Krasheninnikov, A.V., and Sutter, P. (2016). Electron-beam induced transformations of layered tin dichalcogenides. Nano Lett. *16*, 4410–4416. https://doi.org/10.1021/acs.nanolett.6b01541.

Sutter, E., Wang, J., and Sutter, P. (2019a). Nanoparticle-templated thickness controlled growth, thermal stability, and decomposition of ultrathin tin sulfide plates. Chem. Mater. *31*, 2563–2570. https://doi.org/10.1021/acs.chemmater.9b00177.

Sutter, E., Zhang, B., Sun, M., and Sutter, P. (2019b). Few-layer to multilayer germanium(II) sulfide: synthesis, structure, stability, and optoelectronics. ACS Nano *13*, 9352–9362. https://doi.org/10.1021/acsnano.9b03986.

Sutter, P., Ibragimova, R., Komsa, H.-P., Parkinson, B.A., and Sutter, E. (2019c). Self-organized twist-heterostructures via aligned van der Waals epitaxy and solid-state transformations. Nat. Commun. *10*, 5528. https://doi.org/10.1038/s41467-019-13488-5.

Sutter, P., Wang, J., and Sutter, E. (2019d). Wrap-around core–shell heterostructures of layered crystals. Adv. Mater. *31*, 1902166. https://doi.org/10.1002/adma.201902166.

Sutter, P., Wimer, S., and Sutter, E. (2019e). Chiral twisted van der Waals nanowires. Nature *570*, 354–357. https://doi.org/10.1038/s41586-019-1147-x.

Sutter, E., Wang, J., and Sutter, P. (2020a). Lateral heterostructures of multilayer GeS and SnS van der Waals crystals. ACS Nano *14*, 12248–12255. https://doi.org/10.1021/acsnano.0c05978.

Sutter, E., Wang, J., and Sutter, P. (2020b). Surface passivation by excess sulfur for controlled synthesis of large, thin SnS flakes. Chem. Mater. *32*, 8034–8042. https://doi.org/10.1021/acs.chemmater.0c03297.

Sutter, P., Argyropoulos, C., and Sutter, E. (2018). Germanium sulfide nano-optics probed by STEM-cathodoluminescence spectroscopy. Nano Lett. *18*, 4576–4583. https://doi.org/10.1021/acs.nanolett.8b01840.

Sutter, P., Cortes, R., Lahiri, J., and Sutter, E. (2012). Interface formation in monolayer graphene-boron nitride heterostructures. Nano Lett. *12*, 4869–4874. https://doi.org/10.1021/nl302398m.

Sutter, P., Huang, Y., and Sutter, E. (2014). Nanoscale integration of two-dimensional materials by lateral heteroepitaxy. Nano Lett. *14*, 4846–4851. https://doi.org/10.1021/nl502110q.

Sutter, P., French, J.S., Khosravi Khorashad, L., Argyropoulos, C., and Sutter, E. (2021a). Optoelectronics and nanophotonics of vapor–liquid–solid grown GaSe van der Waals nanoribbons. Nano Lett. *21*, 4335–4342. https://doi.org/10.1021/acs.nanolett.1c00891.

Sutter, P., Khorashad, L.K., Argyropoulos, C., and Sutter, E. (2021b). Cathodoluminescence of ultrathin twisted $Ge_{1-x}Sn_xS$ van der Waals nanoribbon waveguides. Adv. Mater. *33*, 2006649. https://doi.org/10.1002/adma.202006649.

Sutter, P., Komsa, H.P., Lu, H., Gruverman, A., and Sutter, E. (2021c). Few-layer tin sulfide (SnS): controlled synthesis, thickness dependent vibrational properties, and ferroelectricity. Nano Today *37*, 101082. https://doi.org/10.1016/j.nantod.2021.101082.

Sutter, P., and Sutter, E. (2013). Microscopy of graphene growth, processing, and properties. Adv. Funct. Mater. *23*, 2617–2634. https://doi.org/10.1002/adfm.201203426.

Sutter, P., and Sutter, E. (2018). Growth mechanisms of anisotropic layered group IV chalcogenides on van der Waals substrates for energy conversion applications. ACS Appl. Nano Mater. *1*, 3026–3034. https://doi.org/10.1021/acsanm.8b00660.

Sutter, P.W., Flege, J.-I., and Sutter, E.A. (2008). Epitaxial graphene on ruthenium. Nat. Mater. *7*, 406–411. https://doi.org/10.1038/nmat2166.

Tanuševski, A., and Poelman, D. (2003). Optical and photoconductive properties of SnS thin films prepared by electron beam evaporation. Solar Energy Mater. Solar Cells *80*, 297–303. https://doi.org/10.1016/j.solmat.2003.06.002.

Tenne, R., Margulis, L., Genut, M., and Hodes, G. (1992). Polyhedral and cylindrical structures of tungsten disulphide. Nature *360*, 444–446. https://doi.org/10.1038/360444a0.

Tizei, L.H.G., Lin, Y.-C., Mukai, M., Sawada, H., Lu, A.-Y., Li, L.-J., Kimoto, K., and Suenaga, K. (2015). Exciton mapping at subwavelength scales in two-dimensional materials. Phys. Rev. Lett. *114*, 107601. https://doi.org/10.1103/PhysRevLett.114.107601.

Tonndorf, P., Schwarz, S., Kern, J., Niehues, I., Del Pozo-Zamudio, O., Dmitriev, A.I., Bakhtinov, A.P., Borisenko, D.N., Kolesnikov, N.N., Tartakovskii, A.I., et al. (2017). Single-photon emitters in GaSe. 2D Mater. *4*, 021010. https://doi.org/10.1088/2053-1583/aa525b.

Tran, K., Moody, G., Wu, F., Lu, X., Choi, J., Kim, K., Rai, A., Sanchez, D.A., Quan, J., Singh, A., et al. (2019). Evidence for moiré excitons in van der Waals heterostructures. Nature *567*, 71–75. https://doi.org/10.1038/s41586-019-0975-z.

Tran, T.T., Bray, K., Ford, M.J., Toth, M., and Aharonovich, I. (2016). Quantum emission from hexagonal boron nitride monolayers. Nat. Nanotechnol. *11*, 37–41. https://doi.org/10.1038/nnano.2015.242.

Voznyi, A., Kosyak, V., Onufrijevs, P., Grase, L., Vecstaudža, J., Opanasyuk, A., and Medvid', A. (2016). Laser-induced SnS_2–SnS phase transition and surface modification in SnS_2 thin films. J. Alloys Compd. *688*, 130–139. https://doi.org/10.1016/j.jallcom.2016.07.103.

Wang, G., Robert, C., Glazov, M.M., Cadiz, F., Courtade, E., Amand, T., Lagarde, D., Taniguchi, T., Watanabe, K., Urbaszek, B., and Marie, X. (2017). In-plane propagation of light in transition metal dichalcogenide monolayers: optical selection rules. Phys. Rev. Lett. *119*, 047401. https://doi.org/10.1103/PhysRevLett.119.047401.

Wang, L., Shih, E.-M., Ghiotto, A., Xian, L., Rhodes, D.A., Tan, C., Claassen, M., Kennes, D.M., Bai, Y., Kim, B., et al. (2020). Correlated electronic phases in twisted bilayer transition metal dichalcogenides. Nat. Mater. *19*, 861–866. https://doi.org/10.1038/s41563-020-0708-6.

Wang, L., Xu, Z., Wang, W., and Bai, X. (2014). Atomic mechanism of dynamic electrochemical lithiation processes of MoS_2 nanosheets. J. Am. Chem. Soc. *136*, 6693–6697. https://doi.org/10.1021/ja501686w.

Wang, W., Leung, K.K., Fong, W.K., Wang, S.F., Hui, Y.Y., Lau, S.P., Chen, Z., Shi, L.J., Cao, C.B., and Surya, C. (2012). Molecular beam epitaxy growth of high quality p-doped SnS van der Waals epitaxy on a graphene buffer layer. J. Appl. Phys. *111*, 093520. https://doi.org/10.1063/1.4709732.

Wang, Z.-J., Weinberg, G., Zhang, Q., Lunkenbein, T., Klein-Hoffmann, A., Kurnatowska, M., Plodinec, M., Li, Q., Chi, L., Schloegl, R., and Willinger, M.-G. (2015). Direct observation of graphene growth and associated copper substrate dynamics by in situ scanning electron microscopy. ACS Nano *9*, 1506–1519. https://doi.org/10.1021/nn5059826.

Whittles, T.J., Burton, L.A., Skelton, J.M., Walsh, A., Veal, T.D., and Dhanak, V.R. (2016). Band alignments, valence bands, and core levels in the tin sulfides SnS, SnS_2, and Sn_2S_3: experiment and theory. Chem. Mater. *28*, 3718–3726. https://doi.org/10.1021/acs.chemmater.6b00397.

Woods, C.R., Withers, F., Zhu, M.J., Cao, Y., Yu, G., Kozikov, A., Ben Shalom, M., Morozov, S.V., van Wijk, M.M., Fasolino, A., et al. (2016). Macroscopic self-reorientation of interacting two-dimensional crystals. Nat. Commun. *7*, 10800. https://doi.org/10.1038/ncomms10800.

Wu, J., Liu, M., Sharma, P.P., Yadav, R.M., Ma, L., Yang, Y., Zou, X., Zhou, X.-D., Vajtai, R., Yakobson, B.I., et al. (2016). Incorporation of nitrogen defects for efficient reduction of CO_2 via two-electron pathway on three-dimensional graphene foam. Nano Lett. *16*, 466–470. https://doi.org/10.1021/acs.nanolett.5b04123.

Wu, M., and Zeng, X.C. (2016). Intrinsic ferroelasticity and/or multiferroicity in two-dimensional phosphorene and phosphorene analogues. Nano Lett. *16*, 3236–3241. https://doi.org/10.1021/acs.nanolett.6b00726.

Xie, S., Tu, L., Han, Y., Huang, L., Kang, K., Lao, K.U., Poddar, P., Park, C., Muller, D.A., DiStasio, R.A., and Park, J. (2018). Coherent, atomically thin transition-metal dichalcogenide superlattices with engineered strain. Science *359*, 1131–1136. https://doi.org/10.1126/science.aao5360.

Xin, C., Zheng, J., Su, Y., Li, S., Zhang, B., Feng, Y., and Pan, F. (2016). Few-layer tin sulfide: a new black-phosphorus-analogue 2D material with a sizeable band gap, odd–even quantum confinement effect, and high carrier mobility. J. Phys. Chem. C *120*, 22663–22669. https://doi.org/10.1021/acs.jpcc.6b06673.

Yang, Y., Li, J., Yin, J., Xu, S., Mullan, C., Taniguchi, T., Watanabe, K., Geim, A.K., Novoselov, K.S., and Mishchenko, A. (2020). In situ manipulation of van der Waals heterostructures for twistronics. Sci. Adv. *6*, eabd3655. https://doi.org/10.1126/sciadv.abd3655.

Yang, Y., Liu, S.-C., Yang, W., Li, Z., Wang, Y., Wang, X., Zhang, S., Zhang, Y., Long, M., Zhang, G., et al. (2018). Air-stable in-plane anisotropic $GeSe_2$ for highly polarization-sensitive photodetection in short wave region. J. Am. Chem. Soc. *140*, 4150–4156. https://doi.org/10.1021/jacs.8b01234.

Ye, G., Gong, Y., Lei, S., He, Y., Li, B., Zhang, X., Jin, Z., Dong, L., Lou, J., Vajtai, R., et al. (2017). Synthesis of large-scale atomic-layer SnS_2 through chemical vapor deposition. Nano Res. *10*, 2386–2394. https://doi.org/10.1007/s12274-017-1436-3.

Yu, J., Xu, C.-Y., Ma, F.-X., Hu, S.-P., Zhang, Y.-W., and Zhen, L. (2014). Monodisperse SnS_2 nanosheets for high-performance photocatalytic hydrogen generation. ACS Appl. Mater. Inter. *6*, 22370–22377. https://doi.org/10.1021/am506396z.

Zang, H., Routh, P.K., Huang, Y., Chen, J.-S., Sutter, E., Sutter, P., and Cotlet, M. (2016). Nonradiative energy transfer from individual CdSe/ZnS quantum dots to single-layer and few-layer tin disulfide. ACS Nano *10*, 4790–4796. https://doi.org/10.1021/acsnano.6b01538.

Zhang, C., Li, M.-Y., Tersoff, J., Han, Y., Su, Y., Li, L.-J., Muller, D.A., and Shih, C.-K. (2018). Strain distributions and their influence on electronic structures of WSe_2–MoS_2 laterally strained heterojunctions. Nat. Nanotechnology *13*, 152–158. https://doi.org/10.1038/s41565-017-0022-x.

Zhang, J., Qu, L., Shi, G., Liu, J., Chen, J., and Dai, L. (2016). N,P-codoped carbon networks as efficient metal-free bifunctional catalysts for oxygen reduction and hydrogen evolution reactions. Angew. Chem. Int. Ed. *55*, 2230–2234. https://doi.org/10.1002/anie.201510495.

Zhang, M., Zhu, Y., Wang, X., Feng, Q., Qiao, S., Wen, W., Chen, Y., Cui, M., Zhang, J., Cai, C., and Xie, L. (2015). Controlled synthesis of ZrS_2 monolayer and few layers on hexagonal boron nitride. J. Am. Chem. Soc. *137*, 7051–7054. https://doi.org/10.1021/jacs.5b03807.

Zhang, Y.J., Ideue, T., Onga, M., Qin, F., Suzuki, R., Zak, A., Tenne, R., Smet, J.H., and Iwasa, Y. (2019). Enhanced intrinsic photovoltaic effect in tungsten disulfide nanotubes. Nature *570*, 349–353. https://doi.org/10.1038/s41586-019-1303-3.

Zhang, Z., Tian, Z., Mei, Y., and Di, Z. (2021). Shaping and structuring 2D materials via kirigami and origami. Mater. Sci. Eng. R: Rep. *145*, 100621. https://doi.org/10.1016/j.mser.2021.100621.

Zhao, B., Wan, Z., Liu, Y., Xu, J., Yang, X., Shen, D., Zhang, Z., Guo, C., Qian, Q., Li, J., et al. (2021). High-order superlattices by rolling up van der Waals heterostructures. Nature *591*, 385–390. https://doi.org/10.1038/s41586-021-03338-0.

Zheng, J., Yan, X., Lu, Z., Qiu, H., Xu, G., Zhou, X., Wang, P., Pan, X., Liu, K., and Jiao, L. (2017). High-mobility multilayered MoS_2 flakes with low contact resistance grown by chemical vapor deposition. Adv. Mater. *29*, 1604540. https://doi.org/10.1002/adma.201604540.

Zhou, X., Tian, Z., Kim, H.J., Wang, Y., Xu, B., Pan, R., Chang, Y.J., Di, Z., Zhou, P., and Mei, Y. (2019). Rolling up $MoSe_2$ nanomembranes as a sensitive tubular photodetector. Small *15*, 1902528. https://doi.org/10.1002/smll.201902528.